Received: 12 July 2022 | Revised: 6 January 2023 | Accepted: 14 February 2023 | Published on: 14 March 2023

DOI: 10.1002/qj.4442

Quarterly Journal of the Royal Meteorological Society RMetS

RESEARCH ARTICLE

Impact of *Aeolus* wind lidar observations on the representation of the West African monsoon circulation in the ECMWF and DWD forecasting systems

Maurus Borne[1] | **Peter Knippertz**[1] | **Martin Weissmann**[2] | **Anne Martin**[3] | **Michael Rennie**[4] | **Alexander Cress**[5]

[1]Institute of Meteorology and Climate Research, Karlsruhe Institute of Technology, Karlsruhe, Germany

[2]Universität Wien, Institut für Meteorologie und Geophysik, Wien, Austria

[3]Ludwig-Maximilians-Universität, Meteorologisches Institut, München Germany

[4]European Centre for Medium-Range Weather Forecasts (ECMWF), Reading, UK

[5]Deutscher Wetterdienst (DWD), Offenbach am Main, Germany

Correspondence
M. Borne, Institute of Meteorology and Climate Research, Karlsruhe Institute of Technology, 76131 Karlsruhe, Germany.
Email: maurus.borne@kit.edu

Abstract

Aeolus is the first satellite mission to acquire vertical profiles of horizontal line-of-sight winds globally and thus fills an important gap in the Global Observing System, most notably in the Tropics. This study explores the impact of this dataset on analyses and forecasts from the European Centre for Medium-Range Weather Forecasts (ECMWF) and Deutscher Wetterdienst (DWD), focusing specifically on the West African Monsoon (WAM) circulation during the boreal summers of 2019 and 2020. The WAM is notoriously challenging to forecast and is characterized by prominent and robust large-scale circulation features such as the African Easterly Jet North (AEJ-North) and Tropical Easterly Jet (TEJ). Assimilating *Aeolus* generally improves the prediction of zonal winds in both forecasting systems, especially for lead times above 24 h. These improvements are related to systematic differences in the representation of the two jets, with the AEJ-North weakened at its southern flank in the western Sahel in the ECMWF analysis, while no obvious systematic differences are seen in the DWD analysis. In addition, the TEJ core is weakened in the ECMWF analysis and strengthened on its southern edge in the DWD analysis. The regions where the influence of *Aeolus* on the analysis is greatest correspond to the Intertropical Convergence Zone (ITCZ) region for ECMWF and generally the upper troposphere for DWD. In addition, we show the presence of an altitude- and orbit-dependent bias in the Rayleigh-clear channel, which causes the zonal winds to speed up and slow down diurnally. Applying a temperature-dependent bias correction to this channel contributes to a more accurate representation of the diurnal cycle and improved prediction of the WAM winds. These improvements are encouraging for future investigations of the influence of *Aeolus* data on African Easterly Waves and associated Mesoscale Convective Systems.

KEYWORDS

aeolus satellite, doppler wind lidar, data assimilation, numerical weather prediction impact, African easterly jet, tropical easterly jet, observing system experiments

1 | INTRODUCTION

Launched on August 22, 2018, *Aeolus* is the second Earth Explorer core mission of the European Space Agency (ESA). The main objective of *Aeolus* is to acquire global atmospheric coverage with high-quality horizontal wind profiles from the surface up to 30 km, which are fundamental for a better understanding of atmospheric dynamics and predictions of weather and climate (Stoffelen *et al.,* 2005). As pointed out by the World Meteorological Organization, the current Global Observing System has a large gap in the spatial and temporal coverage of wind observations, in particular in the Tropics and over ocean areas, which *Aeolus* can fill (Baker *et al.,* 2014). Several impact studies have demonstrated the urgent need for additional wind-profile measurements to reduce uncertainties in initial conditions for numerical weather prediction (NWP) systems, especially above regions with a lack of direct wind observations (Marseille and Stoffelen, 2003; Žagar, 2004; Stoffelen *et al.,* 2005; Stoffelen *et al.,* 2006; Weissmann and Cardinali, 2007; Žagar *et al.,* 2008; Weissmann *et al.,* 2012; Baker *et al.,* 2014). These studies also confirm the particular importance of assimilating wind information in the Tropics, where the lack of geostrophic balance requires simultaneous measurements of wind and mass information.

This study concentrates on impacts of *Aeolus* data on representing the West African Monsoon (WAM) during its peak from June–September in the NWP systems of the European Centre for Medium-Range Weather Forecasts (ECMWF) and Deutscher Wetterdienst (DWD). The WAM was chosen as a study region for the following three reasons. (a) Sparse observations: the conventional station network in tropical Africa is sparse, in particular with respect to radiosondes (Parker *et al.,* 2008; Knippertz *et al.,* 2017), and even existing data are sometimes not transferred to the Global Telecommunication System (GTS) in time for assimilation in global forecasting systems. Moreover, commercial air traffic is limited over tropical Africa, leading to relatively few aircraft reports. In recent years, more satellite observations (e.g. passive microwave sensors and global navigation satellite system (GNSS) radio occultation) complement the conventional observing network, but those observations provide mainly mass information and no direct measurements of wind profiles. (b) Low predictability: NWP models are known to have a poor ability to predict rainfall over West Africa (Fink *et al.,* 2011), barely outperforming ensemble predictions based on climatology (Vogel *et al.,* 2018; Vogel *et al.,* 2021; Walz *et al.,* 2021). One reason for this appears to be the great importance of highly organized mesoscale convective systems (MCSs), which contribute up to 80% of the annual rainfall (Bayo, 1985; Mathon *et al.,* 2002; Fink *et al.,* 2006). It is computationally challenging to achieve the km-scale horizontal resolution that is required for representing these systems explicitly over a large enough model domain (Pante and Knippertz, 2019; Senior *et al.,* 2021), but some improvements have recently been achieved through a more sophisticated convective parametrization (Becker *et al.,* 2021). (c) Socio-economic impact: the West African population is highly reliant on rainfed agriculture and is thus vulnerable to weather extremes, threatening local health, food security, and socioeconomic development Krishnamurthy *et al.* (2014). An improvement in rainfall forecasts may therefore prove beneficial not only for agriculture but also for energy production, water supply, and disease prevention.

Can *Aeolus* become a game changer for a better representation of the WAM in operational systems? *Aeolus* is the first satellite that provides direct wind-profile observations from a Doppler lidar with global coverage. The satellite carries the Atmospheric Laser Doppler Instrument (ALADIN), which uses the Doppler lidar technique to measure wind on the basis of light backscattered from air molecules and particles (Reitebuch, 2012; Lux *et al.,* 2020). A major strength is that the backscattered signal is sampled into two channels: the Rayleigh channel (double Fabry–Pérot spectrometer) for the broadband backscattered signal resulting from Rayleigh–Brillouin scattering by air molecules and the Mie channel (Fizeau spectrometer) for the narrowband backscattered signal from particles and aerosols. The latter is potentially of great importance for the WAM region with its multiple cloud features and aerosol species, such as Saharan dust and smoke from biomass burning (BB). We expect that a potential positive impact could come from improvements to the WAM's most prominent circulation features, the midlevel African Easterly Jet North (AEJ-North) and upper-tropospheric Tropical Easterly Jet (TEJ; Lemburg *et al.,* 2019). The former is characterized by an easterly wind of about 10–15 $m \cdot s^{-1}$ and peaks at 700–600 hPa (Burpee, 1972; Thorncroft and Blackburn, 1999; Nicholson and Grist, 2003; Parker *et al.,* 2005a), and is generated by the temperature gradient between the hot Saharan air and the relatively cool monsoon air from the Gulf of Guinea (Charney and Stern, 1962; Cook, 1999). The AEJ-North is closely linked to the synoptic variability of precipitation, since it supports the formation and propagation of African Easterly Waves (AEWs), which in turn modify moisture transport, stability, and vertical wind shear and thus convective organization (Mohr and Thorncroft, 2006; Janiga and Thorncroft, 2016; Schlueter *et al.,* 2019a,b). The representation of the AEJ-North in the ECMWF model has undergone significant changes in response to model updates and improvements, which have modified the structure and intensity of the jet (Kamga *et al.,* 2000; Tompkins *et al.,* 2005a). The assimilation of

additional observations taken in the framework of field campaigns has unveiled remaining issues: for example, that the AEJ-North is too weak in the ECMWF model over the eastern Sahel (Tompkins *et al.,* 2005b; Agustí-Panareda *et al.,* 2010). The TEJ is commonly described as the southern part of the upper-level Asian monsoon anticyclone and extends from the Indian Ocean to the tropical Atlantic. An improvement of the representation of the WAM system and associated jets may have positive effects on the prediction of tropical cyclones and hurricanes over the Atlantic, which are closely related to AEWs (Brammer and Thorncroft 2015), but also on neighbouring extratropical regions such as the North Atlantic/European sector (Bielli *et al.,* 2010; Gaetani *et al.,* 2011; Pante and Knippertz, 2019) or the Mediterranean basin (Raicich *et al.,* 2003) through teleconnection effects.

Aeolus data have been assimilated operationally at ECMWF since January 2020 and at DWD since May 2020, and a positive impact on the global scale has been demonstrated (Rennie *et al.,* 2021). To achieve this, many instrumental challenges had to be overcome and efforts were made to improve the quality of the data. For example, several systematic and random sources of error—mainly affecting the Rayleigh-clear winds—were identified and corrected, such as biases related to uncorrected "hot pixels" (Weiler *et al.,* 2020), decreasing laser energy, and signal losses in the receiver path (Reitebuch *et al.,* 2019), as well as seasonal temperature variations over the M1 mirror of the receiving telescope (Krisch *et al.,* 2020; Martin *et al.,* 2020; Rennie *et al.,* 2021; Weiler *et al.,* 2021). Although the largest source of Rayleigh-clear Horizontal Line-Of-Sight (HLOS) wind bias could be explained by the telescope mirror temperature-dependent bias (a bias-correction scheme was implemented in the operational processing chain in April 2020), some remaining—not yet fully understood—systematic errors are expected to be present even after reprocessing. In this study we will specifically evaluate the impact of *Aeolus* HLOS wind observations and the effect of the remaining residual observation bias on the WAM circulation in both ECMWF and DWD analyses and forecasts. The remainder of the study is organized as follows. Section 2 introduces the different observing-system experiments (OSEs) investigated in this study and the HLOS wind observation-error modelling and settings, and provides an overview of the data analyzed and verification strategy. In Section 3, we discuss the various atmospheric components and observed circulation features that *Aeolus* captures and the related error structure. This section also contains a description of the influence of *Aeolus* on the AEJ-North and TEJ, with a thorough evaluation of the orbital and channel contributions to the observed influence using background-departure diagnostics. This direct assessment is possible because HLOS winds are more sensitive to the zonal wind, as the lines of sight (LOSs) point around 10° off the zonal direction in the Tropics and can therefore capture the main characteristics of the zonally oriented AEJ-North and TEJ. Section 3 also presents the forecast impact of *Aeolus* on the WAM winds, using background verification against radiosondes and forecast comparisons of zonal wind against ERA5 reanalysis. Finally, Section 4 provides the conclusions and a short outlook on future work.

2 | DATA AND METHODS

2.1 | The *Aeolus* Level 2B product

The *Aeolus* Level 2B (L2B) wind-retrieval software developed by ECMWF and the Royal Netherlands Meteorological Institute (KNMI) provides HLOS wind observations and uncertainty estimates suitable for NWP data assimilation and research purposes (Rennie *et al.,* 2021). Among the various steps within the L2B processor (Rennie *et al.,* 2020), the software corrects for the effect of atmospheric temperature and pressure broadening on the Rayleigh-clear winds to avoid systematic biases (Dabas *et al.,* 2008). Since *Aeolus* does not measure temperature and pressure, the L2B processor utilizes short-range forecasts from ECMWF's Integrated Forecasting System (IFS). The wind observations are categorized as cloudy and cloud-free based on the optical properties of the atmosphere (e.g. the estimated particle scattering ratio, cloud information from the Mie channel) and averaged horizontally over 87 km (Rayleigh-clear) and 12 km (Mie-cloudy) to achieve a good compromise between spatial resolution and signal-to-noise ratio. The L2B product mainly distinguishes between Mie-cloudy and Rayleigh-clear wind retrievals, to avoid contamination of the Rayleigh channel by Mie signals and to improve data quality. Most of the wind data originate from the Rayleigh channel, which is related to the scattering by air molecules. The intensity of the backscattering depends on the concentration of molecules in the atmosphere. The Mie signal depends on the attenuated backscatter of the clouds (Marseille and Stoffelen, 2003) and is strongest at the top of optically thick clouds. Furthermore, high relative humidity leads to a swelling of hygroscopic aerosol particles and therefore an increase in backscatter intensity (Weissmann *et al.,* 2005). Wind data are retrieved in vertical bins with a resolution of 0.25–2 km with profiles having a total of 24 range bins per channel, which are defined by the range-bin settings and can be adjusted depending on the regional topography or climate zone. *Aeolus* mainly measures along the zonal wind direction for the tropical and midlatitude parts

TABLE 1 Overview of the OSEs used in this study.

OSE name	Period	L2B data source	PDGS baseline	Data assimilation system	Bias correction
ECMWF2019 hil4 (Ctrl), hil5 (Exp)	July–September 2019	Reprocessed	2B10	IFS Cycle: 46R1.2. TCO399 ($\Delta x \approx 29$ km)	
ECMWF2019BC hil4 (Ctrl), hldz (Exp)	July–September 2019	Reprocessed	2B10	IFS Cycle: 46R1.2. TCO399 ($\Delta x \approx 29$ km)	Rayleigh-clear temperature-dependent
ECMWF2020 hel1 (Ctrl), hel4 (Exp)	July–September 2020	PDGS NRT dataset	2B10	IFS Cycle: 47R1.1. TCO399 ($\Delta x \approx 29$ km)	
DWD2020 610 (Ctrl), 600 (Exp)	July–September 2020	PDGS NRT dataset	2B10	ICON deterministic R3B07 ($\Delta x \approx 13$ km)	Rayleigh-clear vertically dependent

of the track. The sign convention of the HLOS wind is defined to be negative (positive) when the wind is measured towards (away) the instrument. Because the satellite is in a near-polar, sun-synchronous, dawn–dusk orbit, the overpass over equatorial latitudes is at 06:00 local mean solar time for the descending orbit and 18:00 for the ascending orbit.

For this study, both the reprocessed *Aeolus* L2B product and the ESA Payload Data Ground Segment (PDGS) Near-Real Time (NRT) operational products are used, where a bias correction for M1 mirror temperature variations and additional instrumental drift biases is included. The processing L2B product baselines are discussed in the next section. Our study will focus only on the months of July–September 2019 and 2020, corresponding to the WAM season of the boreal summer.

2.2 | Observing-system experiments (OSEs)

An OSE is a well-established method frequently conducted at NWP centres to study the added value of a given observation type (Bouttier and Kelly, 2001; Kelly *et al.,* 2004). OSEs are, for example, used to assess data from field campaigns (Agustí-Panareda *et al.,* 2010; Harnisch *et al.,* 2011; Weissmann *et al.,* 2011; Schindler *et al.,* 2020; van der Linden *et al.,* 2020) and groups of observations (Cress and Wergen, 2001), and to estimate the benefit of various observation groups (Zapotocny *et al.,* 2002). In an an OSE, two parallel assimilation and forecast experiments are performed, one with and one without assimilation of the observations of interest. The impact of the added data in an OSE is assessed by comparing the accuracy of the forecasts. It is usually expected to have a negative impact when denying a given observation type. In the current study, four OSEs were conducted to evaluate the impact of *Aeolus* L2B data in the DWD global ICOsahedral Nonhydrostatic model (ICON) and the ECMWF IFS covering the boreal summers of 2019 and 2020. The two 2019 OSEs are based on the reprocessed L2B product, while the two 2020 OSEs use the PDG NRT product (see Table 1).

The DWD OSE was performed using the operational version of the global ICON model (Zängl *et al.,* 2015) with a horizontal grid spacing of 13 km (R3B07 grid), 90 vertical levels, and a six-hourly output at 0000, 0600, 1200, and 1800 UTC. The assimilation system is based on a hybrid approach, using a local ensemble transform Kalman filter (LETKF: Hunt *et al.,* 2007; Schraff *et al.,* 2016) to estimate the background uncertainty with an ensemble state, and a three-dimensional variational (3D-VAR) algorithm to achieve a deterministic analysis. This is realized by minimizing a cost function iteratively to fit the model background with observations at their actual time. Additionally to the M1 temperature-dependent bias-correction scheme implemented operationally at DWD, a vertical-latitude-dependent correction based on the previous seven days was applied to the Rayleigh-clear observations before assimilation.

The ECMWF system uses a hybrid ensemble of incremental four-dimensional variational (4D-VAR) assimilation technique (Rabier *et al.,* 2000; Bonavita *et al.,* 2012), which assimilates all observations within a 12-h window. This method ensures that the observations are used in a way dynamically consistent with the model physical processes. Three ECMWF OSEs were conducted using the IFS cycles 46R1.2 and 47R1.1 for the 2019 and 2020 OSEs, respectively, with a 4D outer loop resolution of TCO399, corresponding to a grid spacing of 29 km with 137 vertical layers. In contrast to the DWD OSEs and the operational ECMWF system, only the deterministic analysis was conducted for the OSEs, while the model error estimates were taken from the operational ensemble of data assimilation. The ECMWF2019 OSE was rerun with an

TABLE 2 Summary of the observation-error parameters and error thresholds of the OSEs used in this study. The listed assigned observation errors of DWD are given for the following pressure levels (in hPa): 1000, 850, 700, 500, 400, 300, 250, 200, 150, 100, 70, 50, 30, 20, 10.

NWP centre	Channel	Error threshold ($m \cdot s^{-1}$)	Assigned observation error ($m \cdot s^{-1}$)
ECMWF	Rayleigh-clear	8.5 > 200 hPa	$1.4\sigma_{instr}$
		12 < 200 hPa	
		0 > 850 hPa	
	Mie-cloudy	5	$\sqrt{(1.25^2\sigma^2_{instr} + 2^2)}$
DWD	Rayleigh-clear	7	5.50; 5.00; 4.50; 4.50; 4.75; 5.00; 5.00; 5.25
			5.25; 5.50; 6.00; 6.50; 7.00; 7.50; 8.00
	Mie-cloudy	5	3.50; 3.00; 3.50; 4.00;4.50; 4.75; 5.00; 5.25
			5.25; 5.50; 6.00; 6.00; 6.00; 6.00; 6.00

additional bias correction for Rayleigh-clear data as a function of atmospheric temperature from the ECMWF IFS model, while the two other ECMWF OSEs do not include any bias correction (2019 and 2020). Further description of the ECMWF2019 and ECMWF2020 OSEs can be found in Rennie *et al.* (2021). The systematic comparison between all four OSEs thus allows evaluating the effects of different bias-correction methods in the two different models. Generally, the weight given to an observation in data assimilation is based on the uncertainty associated with its measurement and representativity. Observation minus background (O−B) statistics and Desroziers diagnostics (Desroziers *et al.*, 2005; Rennie *et al.*, 2021) were mainly used to determine the assigned observation errors in the ECMWF and DWD OSEs. The ECMWF OSEs used the following assigned HLOS wind observation-error modelling:

$$\sigma_{ass} = \sqrt{(\alpha^2\sigma^2_{instr} + \sigma^2_{repr})}, \quad (1)$$

with α the L2B processor instrument-error estimate scaling factor, which accounts for important noise terms that are missing in the L2B estimated error, σ_{instr} the L2B processor reported instrument-error standard deviation, which has the advantage of capturing drifting signal levels in the range-bin thickness, and σ_{repr} the representativeness-error standard deviation. In contrast, the assigned observation error in the DWD OSE is estimated using a lookup table for specific altitude levels and interpolation between levels. An important step in preprocessing the data is the quality control of the L2B product, which verifies the validity of the measurement and corresponding errors. Only Rayleigh-clear or Mie-cloudy winds with a valid confidence flag and below a specific error threshold are assimilated. More information about the assigned observation-error parameters and error thresholds can be found in Table 2.

2.3 | Verification strategy

A common tool for assessing observation quality is the use of departures between observations (O) and short-range forecasts (B). They can be used to estimate systematic and random errors in the observation, background, and analysis fields, and are an essential part of quality control in NWP centres (Hollingsworth *et al.*, 1986). This procedure can also be applied to forecast ranges beyond 12 h, which are considered sufficiently independent of the observation against which they are verified.

To assess the impact of *Aeolus* on WAM circulation features, we compute the standard root-mean-square error (RMSE) according to the following equation:

$$RMSE = \sqrt{\frac{1}{M}\sum_{m=1}^{M}(x^f_m - x^r_m)^2}, \quad (2)$$

with x^f the forecast value, x^r the reference value against which the forecast is verified, and M the number of data pairs. In both OSEs, forecasts are verified against the ERA5 reanalysis (Hersbach *et al.*, 2020), which is a robust and relatively independent reference, as *Aeolus* is not assimilated in this dataset. ERA5 comprises additional satellite and in situ observations not considered in the OSEs. The ERA5 product is constructed using an older version of the IFS 4D-var, namely CY41R2 with a resolution of 31 km. Output is provided on 37 interpolated pressure levels. We calculate the RMSE for the zonal wind over West Africa for both *Aeolus* and control experiments, and evaluate the improvement by calculating the relative difference in RMSE. To characterize the atmospheric constituents that influence the *Aeolus* measurements, cloud fraction from ERA5 and aerosol mixing ratio products from the Copernicus Atmosphere Monitoring Service

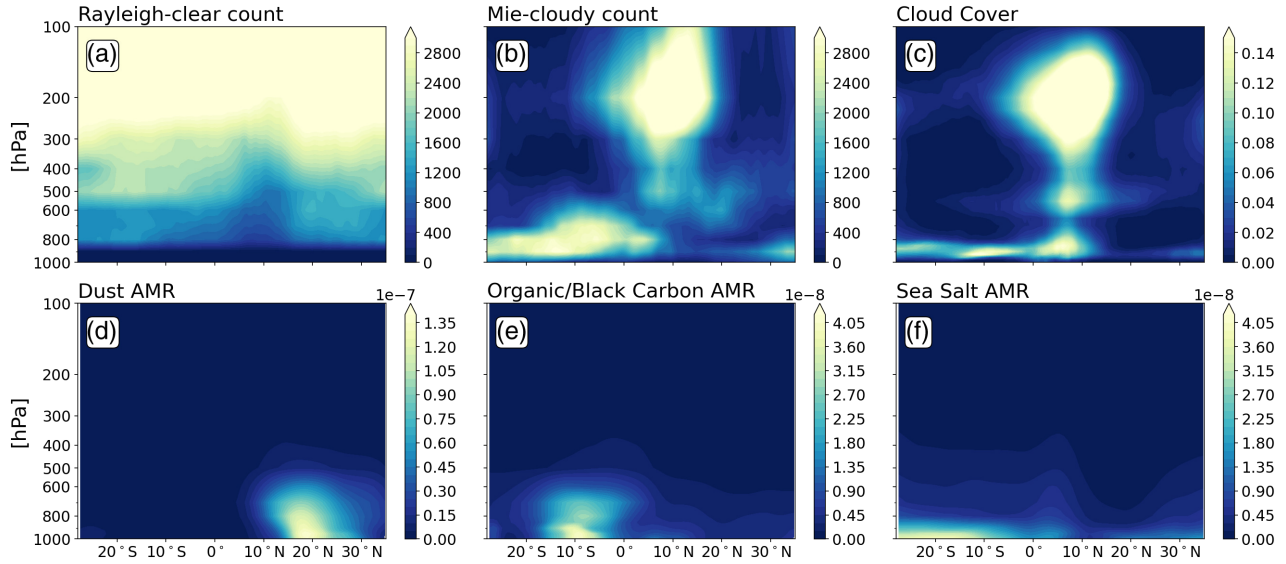

FIGURE 1 Latitude–height cross-sections of counts for *Aeolus* (a) Rayleigh-clear and (b) Mie-cloudy measurements, as well as (c) ERA5 cloud cover, (d) CAMS dust aerosol (0.03–20 μm) mixing ratio, (e) CAMS organic matter and black carbon aerosol mixing ratio, and (f) CAMS sea-salt aerosol (0.03–20 μm) mixing ratio. AMR stands for aerosol mixing ratio. The fields are averaged between 30°W and 30°E during the July–September 2019 period. [Colour figure can be viewed at wileyonlinelibrary.com]

(CAMS) global atmospheric composition and prediction (Benedetti *et al.*, 2009; Morcrette *et al.*, 2009) are used. The model employed for the CAMS prediction of global atmospheric composition is the IFS, which uses the CY47R2 4D-var cycle corresponding to a horizontal resolution of 40 km with output on 25 pressure levels.

3 | RESULTS AND DISCUSSION

This section presents the main results of this study in three subsections. The first one (Section 3.1) examines the distribution of observations in the Rayleigh-clear and Mie-cloudy channels, shows the resulting climatologies, and discusses the assigned observation and background errors in the different OSEs. Section 3.2 analyzes the impact of *Aeolus* data on 3D analysis fields with a special emphasis on the contributions from the two orbit phases and the two channels as well as the effect of the bias correction tested at ECMWF for 2019. Finally, Section 3.3 presents the impact of *Aeolus* data on 1–4 day forecasts, with a special emphasis on predictions of the AEJ-North and TEJ. This analysis is supplemented by a verification of the model background with radiosondes over Africa.

3.1 | Observed atmospheric features

West Africa during boreal summer is characterized by many different types of aerosols and clouds that affect the *Aeolus* measurements. Figure 1 shows longitudinal averages between 30°E and 30°W of the number of counts for both Rayleigh-clear and Mie-cloudy channels from the ECMWF2019 OSE, as well as mixing ratios of different aerosol types from the CAMS and cloud fraction from ERA5 during the boreal summer of 2019. Irrespective of latitude, the Rayleigh-clear counts (Figure 1a) peak in the upper troposphere and lower stratosphere with values around 3000. Counts below 300 hPa are markedly reduced around the cloudy Intertropical Convergence Zone (ITCZ), which reaches its northernmost position in August at about 11°N and is often referred to as the African rainbelt (Nicholson, 2009). There are also indications for slightly reduced counts at midlevels towards the subtropical ends of the study domain in both hemispheres. Rayleigh-clear data below 850 hPa are rejected at ECMWF, as the impact found there was slightly negative. (see Table 2). The more complex Mie-cloudy signal (Figure 1b) is shaped by the distribution of clouds and aerosols. There is a distinct maximum in the upper troposphere between 300 and 100 hPa over the African rainbelt around 10°N, corresponding to returns from cumulonimbus clouds, their associated anvils, or optically thick cirrus. The corresponding maximum in cloud fraction can be seen in Figure 1c. In this area, Rayleigh-clear and Mie-cloudy counts are of a similar magnitude, exceeding 3000 counts (cf. Figure 1a,b). During the ascending orbit at 1800 UTC (not shown here), there is a higher number of Mie-cloudy counts over this location, caused by the stronger land convection occurring in the afternoon. Below the prominent high cloud maximum, two smaller peaks are evident in Figure 1c, likely corresponding to early stages of

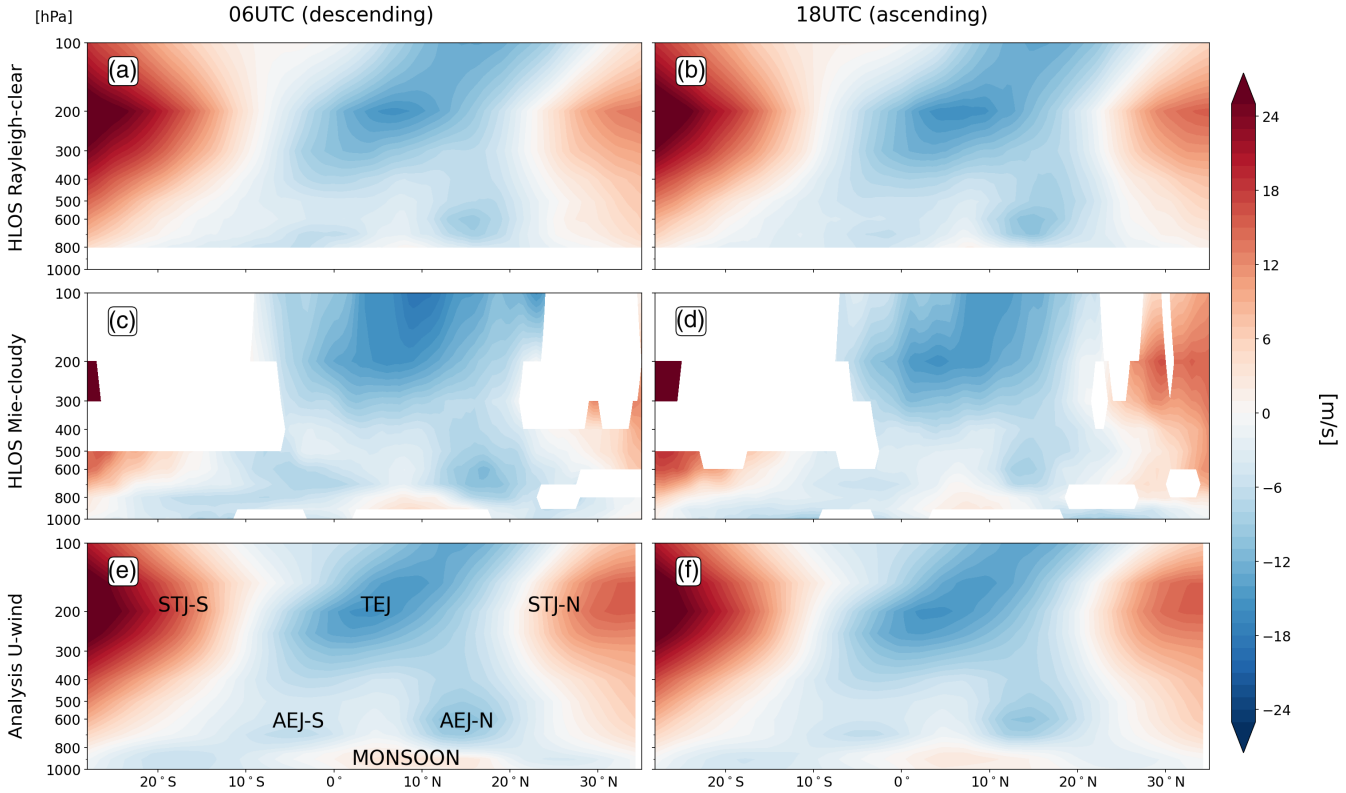

FIGURE 2 Latitude–height cross-sections of *Aeolus* measured (a,b) Rayleigh-clear and (c,d) Mie-cloudy HLOS winds, as well as (e,f) zonal wind from the ECMWF2019 analysis that includes *Aeolus* data. Shown are 0600 UTC (left column) and 1800 UTC (right column), corresponding to the descending and ascending orbits, respectively. The fields are averaged between 30°W and 30°E and smoothed using a latitudinal moving average of 2° grid size for the period July–September 2019. Regions for which no wind data were collected are shown in white. The major jet features of the African Easterly Jet North (AEJ-N) and South (AEJ-S), Tropical Easterly Jet (TEJ), and Subtropical Jets North (STJ-N) and South (STJ-S), as well as the southwesterly monsoon flow, are labelled in (e). HLOS winds from the descending track are multiplied by −1 to correspond with the sign convention of the model coordinate system. [Colour figure can be viewed at wileyonlinelibrary.com]

cumulonimbus, cumulus congestus, or altocumulus layers just below 500 hPa and boundary-layer clouds below 800 hPa (Johnson *et al.*, 1999). These, however, are less prominent in Mie-cloudy counts (Figure 1b) due to attenuation effects. Higher counts at midlevels extend northwards from the rainbelt region into the Sahara. These appear to be partly related to midlevel clouds (Figure 1c) and to the high dust content of the dry and warm Saharan Air Layer (SAL: Figure 1d; Dunion and Marron, 2008). The SAL is mainly sampled in its upper parts by Mie-cloudy scattering (Figure 1b). To the south of the African rainbelt, a distinct low-level maximum is evident stretching from 30°S to 5°N (Figure 1b). The southern part is restricted to levels below 700 hPa, but around 8°S enhanced counts reach up to about 550 hPa. This maximum is likely due to a combination of sea-salt aerosol in the shallow marine boundary layer (Figure 1f, below 900 hPa), low mostly stratiform clouds at the top of the boundary layer (Figure 1c, below 800 hPa) as described, for example, in Knippertz *et al.* (2011) and Schrage and Fink (2012), and a relatively deep plume of BB aerosol, as indicated by enhanced levels of black carbon and organic matter (Figure 1e, around 10°S: Reid *et al.*, 2005; Levin *et al.*, 2010; Zuidema *et al.*, 2016; Carter *et al.*, 2021). This plume originates from agricultural and forest burning (Barbosa *et al.*, 1999; Haslett *et al.*, 2019), with some parts getting thermally lifted above the low-level clouds. Taking Rayleigh-clear and Mie-cloudy signals together, most parts of the WAM region show a satisfactory level of sampling such that the main circulation features should be captured by *Aeolus* measurements.

Since the WAM region is located around the Greenwich meridian, the *Aeolus* descending and ascending observations are included in the 0600 UTC and 1800 UTC assimilation windows, respectively.

Figure 2 compares the HLOS winds for ascending and descending orbits with the zonal wind of the analysis field of the ECMWF2019 OSE where *Aeolus* is assimilated. The Rayleigh-clear HLOS wind observations (Figure 2a,b) can represent all important wind features well above

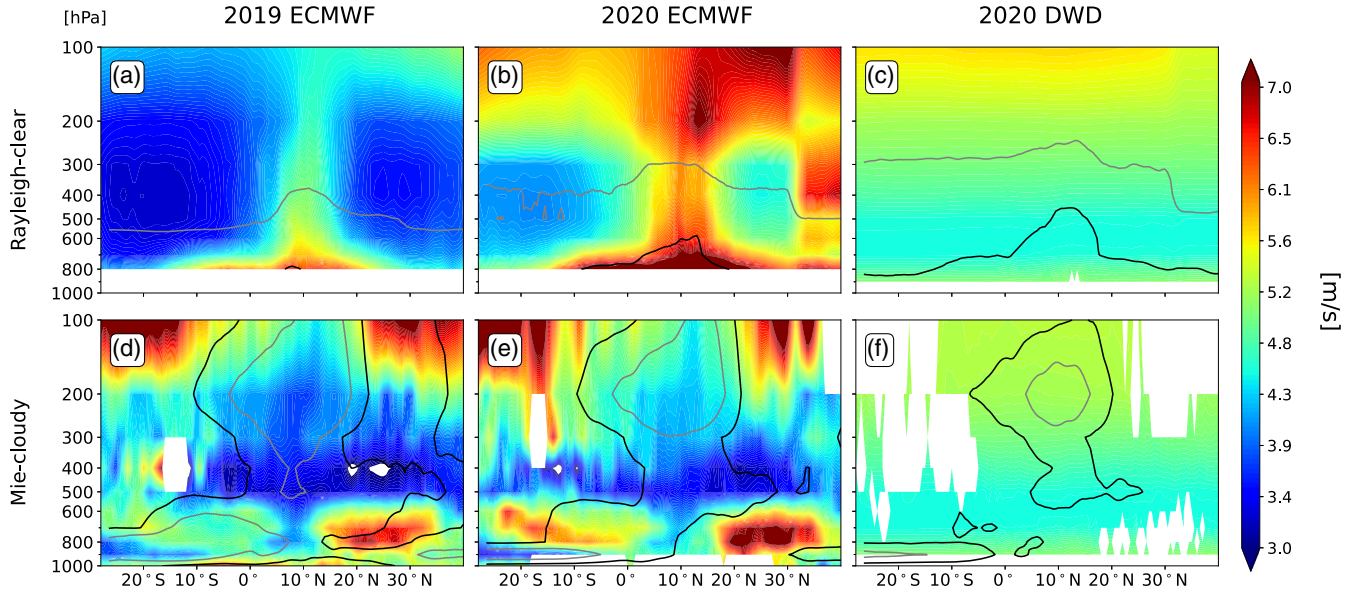

FIGURE 3 Latitude–height cross-sections of Rayleigh-clear (top row) and Mie-cloudy (middle row) assigned observation error for ECMWF2019 (left column), ECMWF2020 (middle column), and DWD2020 (right column), all for July–September. The fields are averaged between 30°W and 30°E and smoothed using a latitudinal moving average of 2° grid size for the period July–September 2019. Regions for which no wind data were collected are shown in white. The grey and black contours correspond to 1500 and 500 measurement counts, respectively. The lines in panels (a) and (b) here correspond to the shading in Figure 1a,b. [Colour figure can be viewed at wileyonlinelibrary.com]

850 hPa, i.e. the TEJ around 5°N and the subtropical jets of both hemispheres in the upper troposphere, as well as the AEJ-North (10–15°N, between 700 and 500 hPa) and AEJ-South (5°S, ~800 hPa) in the midtroposphere (see labels in Figure 2e). Rayleigh-clear winds are generally consistent between ascending (Figure 2a) and descending (Figure 2b) orbits, although some differences in the intensity of the TEJ and AEJ-North are visible, and can possibly be attributed to either diurnal cycle effects between dusk (1800 UTC) and dawn (0600 UTC) or orbit-dependent biases. The Mie-cloudy observations (Figure 2c,d) have too few measurements in the usually cloud- and aerosol-free areas of the subtropical jets (see Figure 1), but can capture the TEJ, the AEJ-North, and partially the AEJ-South, as well as the westerly component of the monsoon flow between 0 and 15°N at 900 hPa. Differences between the orbits are again noteworthy, with the intensity of the AEJ-North and the TEJ stronger near 100 hPa at 0600 UTC (Figure 2c) compared with 1800 UTC (Figure 2d). Furthermore, Mie-cloudy winds have a much larger TEJ jet core with respect to Rayleigh-clear winds. According to Lemburg *et al.* (2019), cloud-related processes such as convection and the change in diabatic heating/cooling due to radiation have an influence on the TEJ. In general, the TEJ is expected to strengthen a few hours after a large-scale convective event, mainly southwest of the convection, which is consistent with the stronger TEJ observed in Mie-cloudy winds. Finally, the HLOS Rayleigh-clear winds (Figure 2a,b) seem to have the best agreement with the analysis field (Figure 2e,f) in terms of the pattern and intensity of the different jets, while Mie-cloudy seems to have a stronger TEJ compared with the analysis. The largest impact of *Aeolus* data on analysis fields is expected in regions with high data density, low assigned observation errors, and large background errors.

Figure 3 shows both the Rayleigh-clear and Mie-cloudy assigned observation errors for the three OSEs without bias correction. The assigned observation error in the ECMWF OSEs is mainly derived from the instrument-error estimate of the L2B processor, while in the DWD OSE it is determined by a predefined lookup table (see Table 2). For ECMWF2019, the assigned Rayleigh-clear observation error has minima around 2.8 $m \cdot s^{-1}$ in the free troposphere in the southern and northern parts of the study domain (Figure 3a). Errors increase markedly in the area of the African rainbelt (around 10°N), where they exceed 5 $m \cdot s^{-1}$ at lower levels. Here, the number of counts is reduced, as indicated by the grey line in Figure 3a (see full field in Figure 1c). The increase in error can be attributed to the lower signal-to-noise ratio in broken cloud scenes (see Figure 1c). In addition, there is a general increase in the upper troposphere above 200–150 hPa, which is likely related to cirrus clouds, and below 600 hPa in areas where clouds and aerosol are abundant (see Figure 1c–f). The corresponding analysis for 2020 (Figure 3b) shows some similarities in terms of the overall pattern but generally much higher values exceeding 5 $m \cdot s^{-1}$ in large parts of the domain. This may be attributed to the decreasing

atmospheric path signal and thinner range-bin settings, increasing the Rayleigh-clear wind random error (Reitebuch *et al.*, 2020). As indicated by the grey and black lines in Figure 3b, this also leads to an overall reduced number of counts. The DWD experiment for 2020 (Figure 3c), in contrast, assumes a much smoother error pattern that reveals the height dependence of the assigned error. The error is generally lower and does not exceed 5 $m \cdot s^{-1}$ anywhere in the domain. DWD does consider data from below 850 hPa, but overall fewer observations than in ECMWF pass the initial quality control, as indicated by the grey and black lines in Figure 3c.

The corresponding observation errors for Mie-cloudy winds show a different and generally more noisy structure for both ECMWF experiments (Figure 3d,e). Errors are larger in regions dominated by aerosols (i.e., BB and SAL) than in regions dominated by clouds (see Figure 1c–f). Mie-cloudy backscatter from ice particles and cloud droplets generally has a stronger signal level, while backscatter from aerosol layers is weaker, thus increasing the wind errors. The representativeness error of Mie-cloudy winds may also depend on the spectral properties and concentration of the various atmospheric constituents. As for the Rayleigh signals, the assigned error for DWD and the number of counts used (Figure 3f) are overall smaller than for ECMWF. The error is dominated by the height dependence, giving overall similar values for Mie-cloudy and Rayleigh-clear winds (cf. Figure 3c,f).

3.2 | Influence on analysis fields

3.2.1 | Mean and root-mean-squared differences

To investigate the influence of *Aeolus* on the representation of WAM wind subsystems such as the AEJ-North and TEJ in the analysis fields, mean differences (MDs) and root-mean-square differences (RMSDs) in the zonal wind component were computed for all four OSEs (see Table 1) with four times daily data. Figure 4 shows these quantities as latitude–height cross-sections averaged between 30°W and 30°E, while Figure 5 shows corresponding horizontal maps at levels characteristics of the AEJ-North (700 hPa) and TEJ (200 hPa). To locate the position of the jets, grey and black lines are drawn in both figures for zonal wind speeds of 6 and 9 $m \cdot s^{-1}$, respectively.

For the ECMWF OSEs, the largest MD and RMSD (top three rows in Figure 4) correspond to the convective ITCZ and the cumulonimbus outflow region, where the background forecast error is largest (not shown), while for the DWD2020 OSE (bottom row in Figure 4) even more significant differences are present in the upper tropical troposphere centred on the Equator south of the cumulonimbus outflow region. The ECMWF2019 OSE shows a strengthening of the central region of the TEJ (Figures 4a, 5b) by up to 0.4 $m \cdot s^{-1}$ and a weakening of the same magnitude south of the AEJ-North, corresponding to the region where Mie-cloudy captures congestus and altocumulus clouds (see Figure 1b,c). These changes are accompanied by large random changes in wind (Figure 4b) when *Aeolus* is assimilated. These features are also evident in Figure 5, with maximum weakening occurring south of the AEJ-North between 25°W and 15°E at 10°N, notwithstanding a strengthening of the AEJ-North towards the eastern part of the Sahel (~ 20°E: Figure 5a). The strengthening of the northern part of the AEJ-South (Figures 4a, 5a), associated with a change in wind direction between the monsoon layer and the mean easterly winds, is also striking. For the TEJ, the strengthening is apparent across the entire jet (Figure 5b). In comparison, the ECMWF2019BC OSE shows an almost identical influence of *Aeolus* on the analysis (Figures 4a–d, 5a–h), implying that the temperature-dependent bias correction of the Rayleigh channel does not contribute noticeably to the analysis differences averaged at four times per day. The influence of *Aeolus* on the ECMWF2020 OSEs is similar to that of the ECMWF 2019 OSEs, with a comparable strengthening of the TEJ of ~0.4 $m \cdot s^{-1}$ but a less pronounced weakening of the southern edge of the AEJ-North of only ~0.2 $m \cdot s^{-1}$ and no obvious strengthening of the AEJ-North over the eastern Sahel (Figures 4e, 5i,j). It is noteworthy that the maximum RMSD in the ECMWF 2019 OSEs affects the upper part of the TEJ between 200 and 100 hPa and between 700 and 300 hPa (Figure 4b–d), while in the ECMWF2020 OSE it spans the entire ITCZ region between 700 and 100 hPa (Figure 4f), thus explaining the weaker RMSD at 200 hPa in 2019 (Figure 5d–h) compared with 2020 (Figure 5l). Moreover, the influence in the DWD2020 OSE is much larger, with a slowdown of the southern edge of the TEJ of more than 0.5 $m \cdot s^{-1}$ and a less pronounced acceleration of ~0.2 $m \cdot s^{-1}$ of the northern part of the TEJ (Figures 4g, 5m–n). The strong deceleration is accompanied by more significant random changes in the zonal wind fields due to *Aeolus* compared with the ECMWF OSEs (Figures 4h, 5o–p). Furthermore, the DWD2020 OSE does not show a significant change in the structure of AEJ-North, likely due to a relatively low background forecast error in the domain, which gives more weight to the background in the analysis.

Finally, we assess to what extent *Aeolus* assimilation brings the analyses of ECMWF2020 and DWD2020 together. Figure 6a,b depicts the difference between ECWMF2020 and DWD2020 analyses with and without *Aeolus*, respectively, while Figure 6c shows the differences between Figure 6a and b. The black and red lines

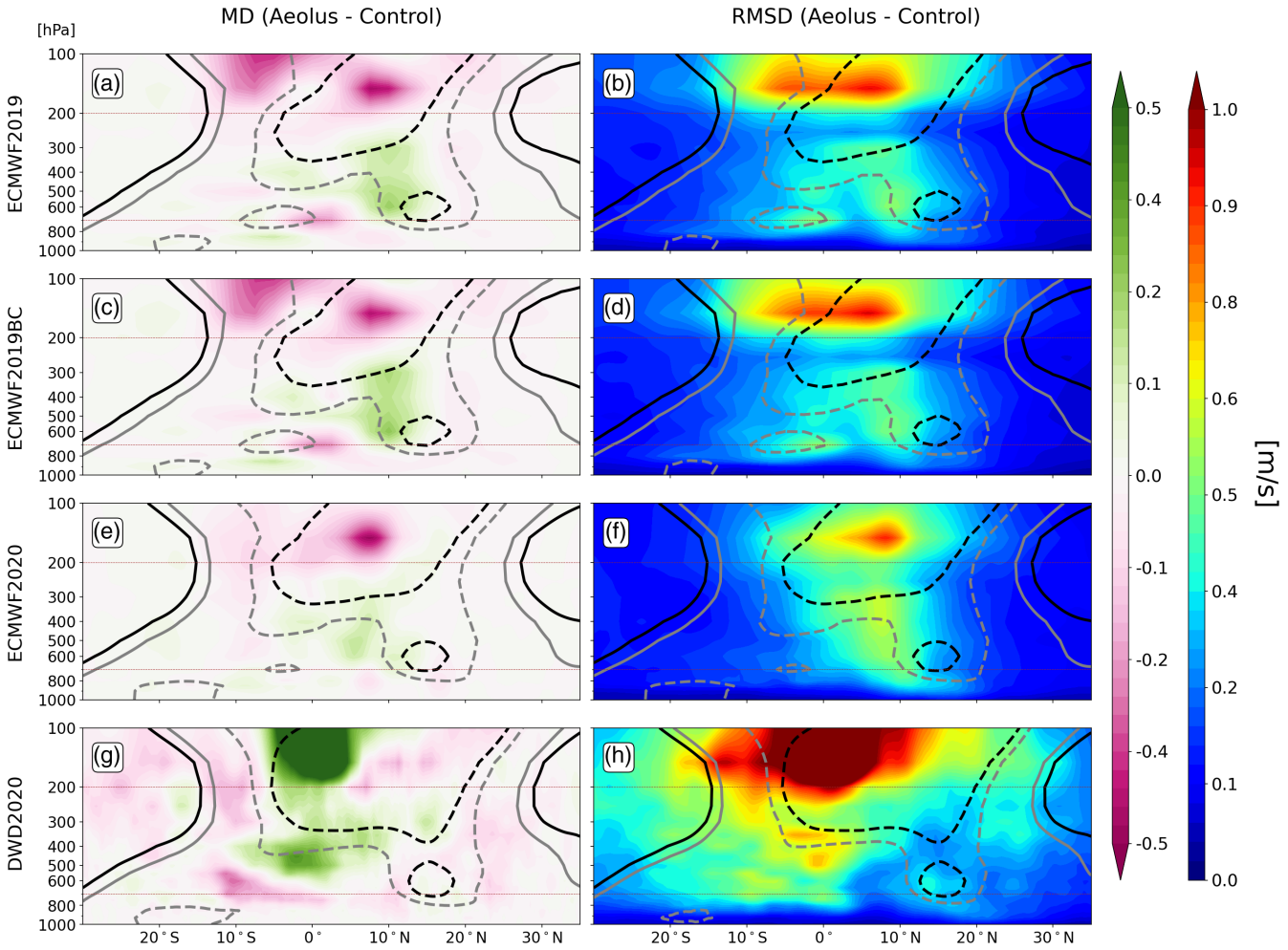

FIGURE 4 Latitude–height cross-sections of mean difference (MD, left column) and root mean square difference (RMSD, right column) between the analysis fields of the zonal wind component *Aeolus* minus Control for the four different OSEs (see Table 1). The fields are averaged between 30°W and 30°E during July–September. The grey and black contours correspond to zonal wind fields, taken from the OSE with *Aeolus*, of 6 and 9 $m \cdot s^{-1}$, respectively. Solid lines indicate westerlies, dashed ones easterlies. The brown lines mark the 200 and 700 hPa levels. [Colour figure can be viewed at wileyonlinelibrary.com]

represent the wind fields at 9 $m \cdot s^{-1}$ in the ECMWF and DWD analysis with *Aeolus*, respectively. In general, the differences between ECMWF and DWD analyses are larger (Figure 6a,b, up to 4 $m \cdot s^{-1}$) than the differences induced by the assimilation of *Aeolus* (Figure 6c, up to 1.5 $m \cdot s^{-1}$ exceeding the colour bar). The most significant differences between ECMWF and DWD model analyses are found in the area of the TEJ, with DWD revealing a stronger TEJ of up to 4 $m \cdot s^{-1}$ compared with ECWMF. The AEJ-North, however, seems to be relatively consistent between the ECMWF and DWD. Figure 6c shows that the convective ITCZ above 600 hPa, culminating at the southern edge of the TEJ, is the region where ECMWF and DWD converge most when *Aeolus* is assimilated. Elsewhere, especially in regions dominated by clear-sky conditions, the analyses diverge by up to 0.2 $m \cdot s^{-1}$. These differences appear to follow the Rayleigh-clear and Mie-cloudy measurement regions, with the Mie-cloudy observations in the convective ITCZ seemingly bringing the two model analyses closer together, while the Rayleigh-clear measurements pulls them apart. The additional vertical bias correction included in the Rayleigh-clear channel in the DWD2020 OSE could explain the observed discrepancies in clear-sky regions.

3.2.2 | Orbital phase and channel contributions

In this subsection we use statistics of observation minus background (O−B) departures to disentangle the contributions of the HLOS Rayleigh-clear and Mie-cloudy wind observations to the analysis differences discussed in the previous subsection. Data corresponding to ascending and

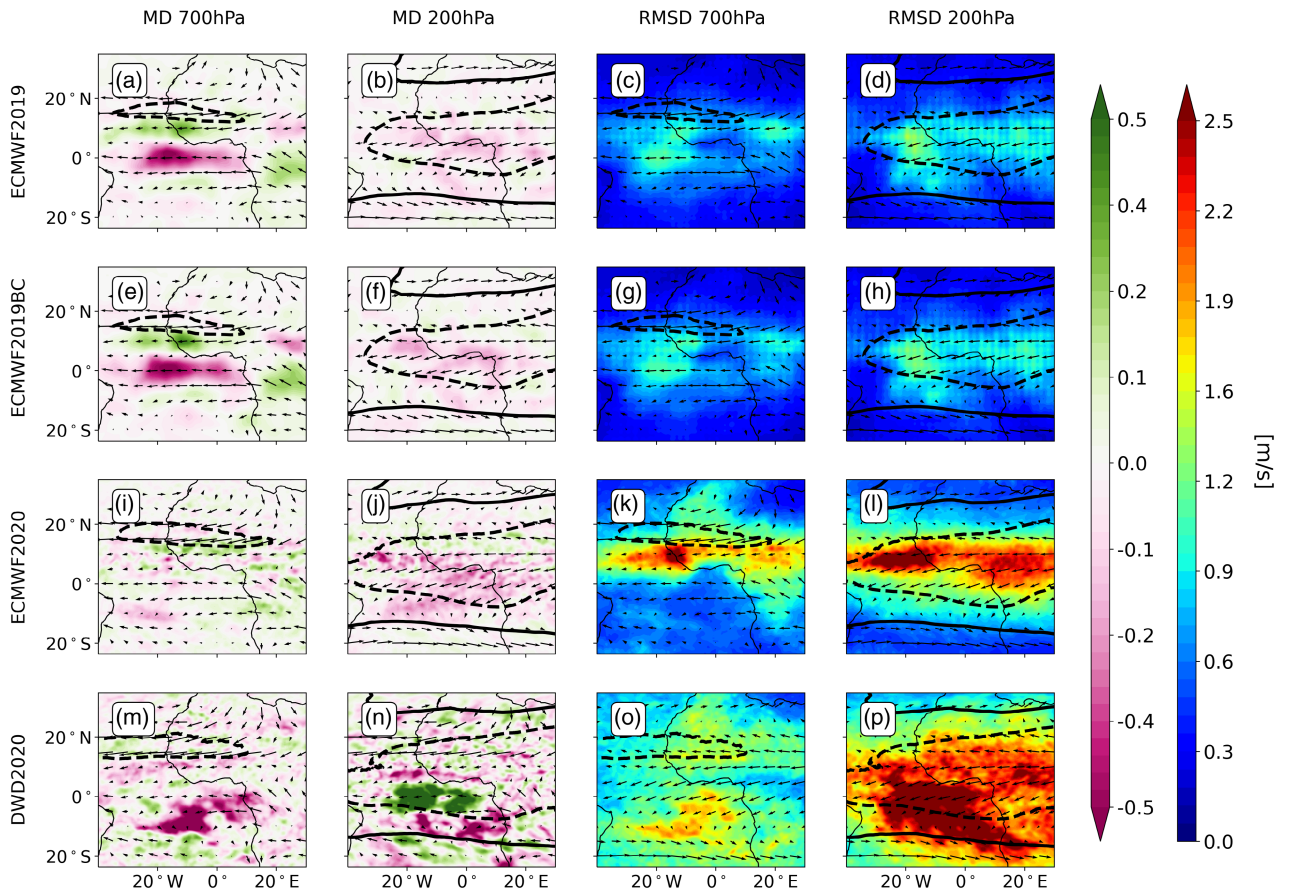

FIGURE 5 Horizontal maps of the July–September mean differences (MD, left two columns) and root-mean-square differences (RMSD, right two columns) between the analysis fields of the zonal wind component *Aeolus* minus Control for the four different OSEs (see Table 1). The black contours show the 9 m·s^{-1} zonal wind isotach from the analysis with *Aeolus*. Solid lines indicate westerlies, dashed ones easterlies. The AEJ-North is evident at 700 hPa, while the TEJ and STJs are visible at 200 hPa. [Colour figure can be viewed at wileyonlinelibrary.com]

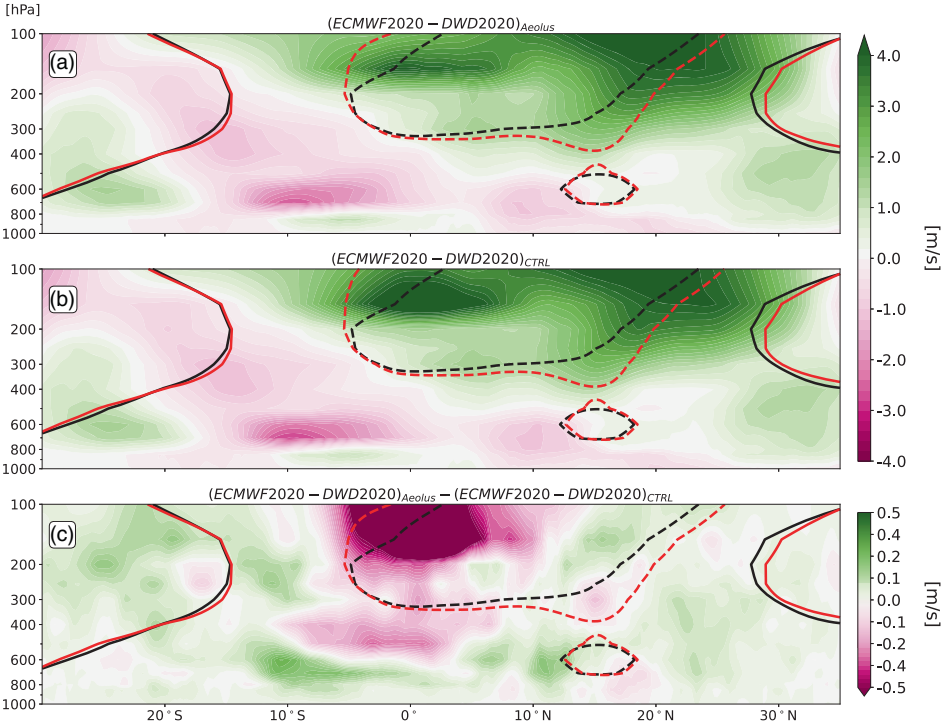

FIGURE 6 Latitude–height cross-sections of the mean difference between the analysis fields of the zonal wind component of ECMWF2020 minus DWD2020 (a) with and (b) without *Aeolus*, as well as (c) the difference between both differences. The fields are averaged between 30°W and 30°E during July–September. The black and red contours correspond to zonal wind fields, taken from the OSE with *Aeolus* at 9 m·s^{-1} for the ECMWF and DWD OSEs, respectively. Solid lines indicate westerlies, dashed ones easterlies.

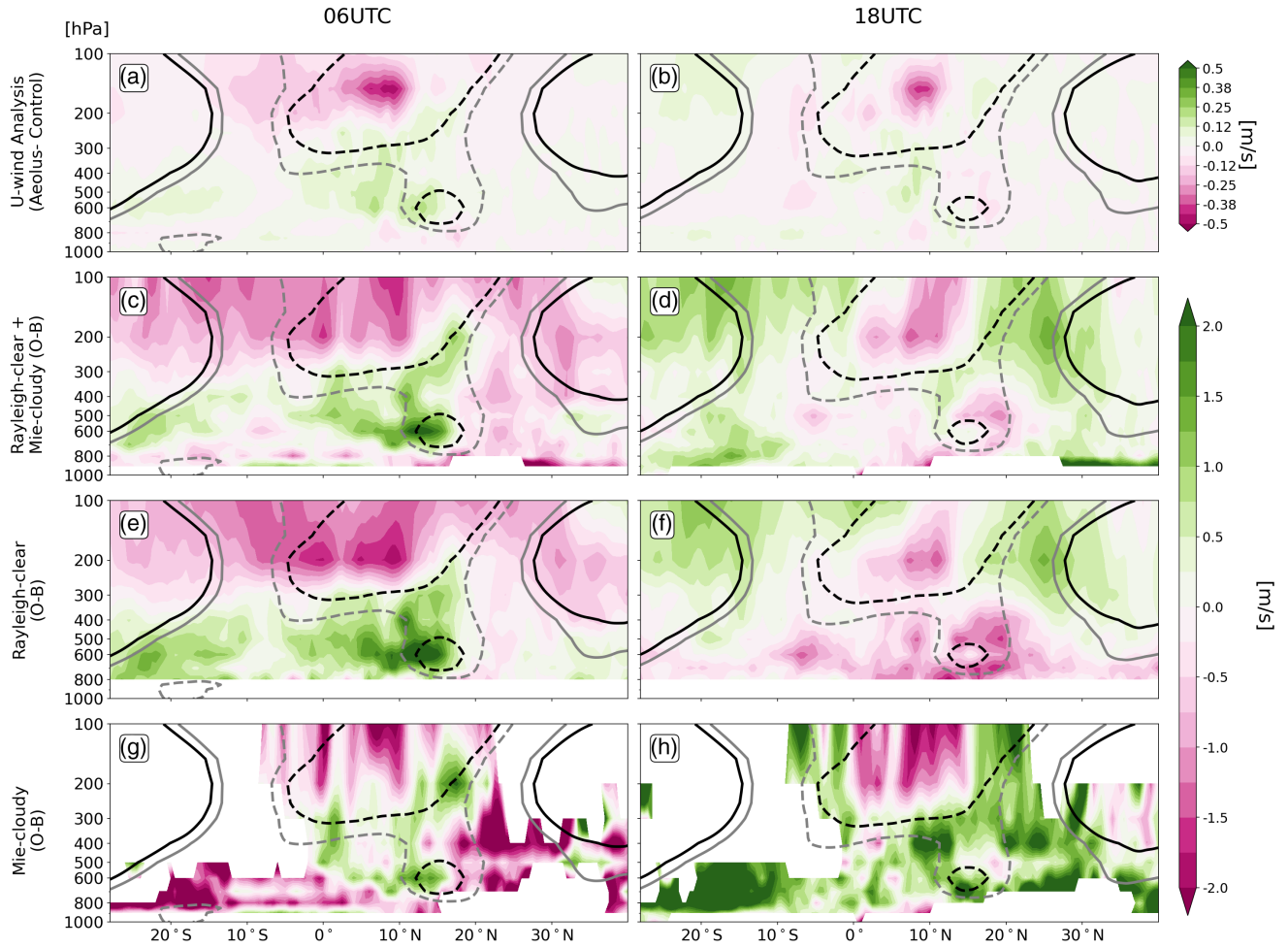

FIGURE 7 Latitude–height cross-sections showing July–September mean differences between the analysis fields of the zonal wind component *Aeolus* minus Control from the ECMWF2020 OSE at (a) 0600 UTC and (b) 1800 UTC. Subsequent panels show corresponding HLOS first guess-departures for (c,d) Rayleigh-clear and Mie-cloudy combined, (e,f) Rayleigh-clear, and (g,h) Mie-cloudy. All fields are averaged between 30°W and 30°E. The grey and black contours correspond to zonal wind fields of 6 and 9 $m \cdot s^{-1}$, respectively, from the analysis with *Aeolus*. Solid lines indicate westerlies, dashed ones easterlies. HLOS winds from the descending track are multiplied by −1 to correspond to the sign convention of the model coordinate system. [Colour figure can be viewed at wileyonlinelibrary.com]

descending tracks will be examined separately to reveal the effects of the orbit phase. For the ECMWF2020 OSE, Figure 7a,b shows the analysis differences *Aeolus* minus control at 0600 UTC (descending orbit) and 1800 UTC (ascending). These two panels can be compared with Figure 4e directly and use the same shadings and lines. The comparison reveals that the total difference between the analyses with and without *Aeolus* data is dominated by 0600 UTC, where the strengthening of the TEJ (plus a southward extension of negative differences) and the weakening of the southern edge of the AEJ-North are more pronounced. Signals in the Northern Hemisphere subtropics are generally small, while in the Southern Hemisphere small-amplitude differences at 0600 UTC and 1800 UTC of opposite sign largely cancel each other out.

The subsequent panels of Figure 7 (i.e., c–h) show background departures for the two *Aeolus* channels and their combination to examine where the diurnal differences in the *Aeolus* impact on the analysis fields come from. The O−B data of Rayleigh-clear and Mie-cloudy combined (Figure 7c,d) have overall structures similar to their analysis counterparts but with amplitudes about 4–10 times larger, revealing considerable diurnal variations, as already discussed in the context of Figure 2. The magnitude of the influence on the analysis is a clear reflection of the assigned errors (see Figure 3b,e,h). For example, the negative HLOS differences at upper levels in the TEJ region, where background errors are assumed to be relatively large (Figure 3h), translate into a strong signal in the analysis at 0600 UTC (cf. Figure 7a,c), while similar HLOS differences in the southern subtropics, where background errors are small, have very little impact.

Separating the Rayleigh-clear and Mie-cloudy contributions reveals that the combined O−B structures are

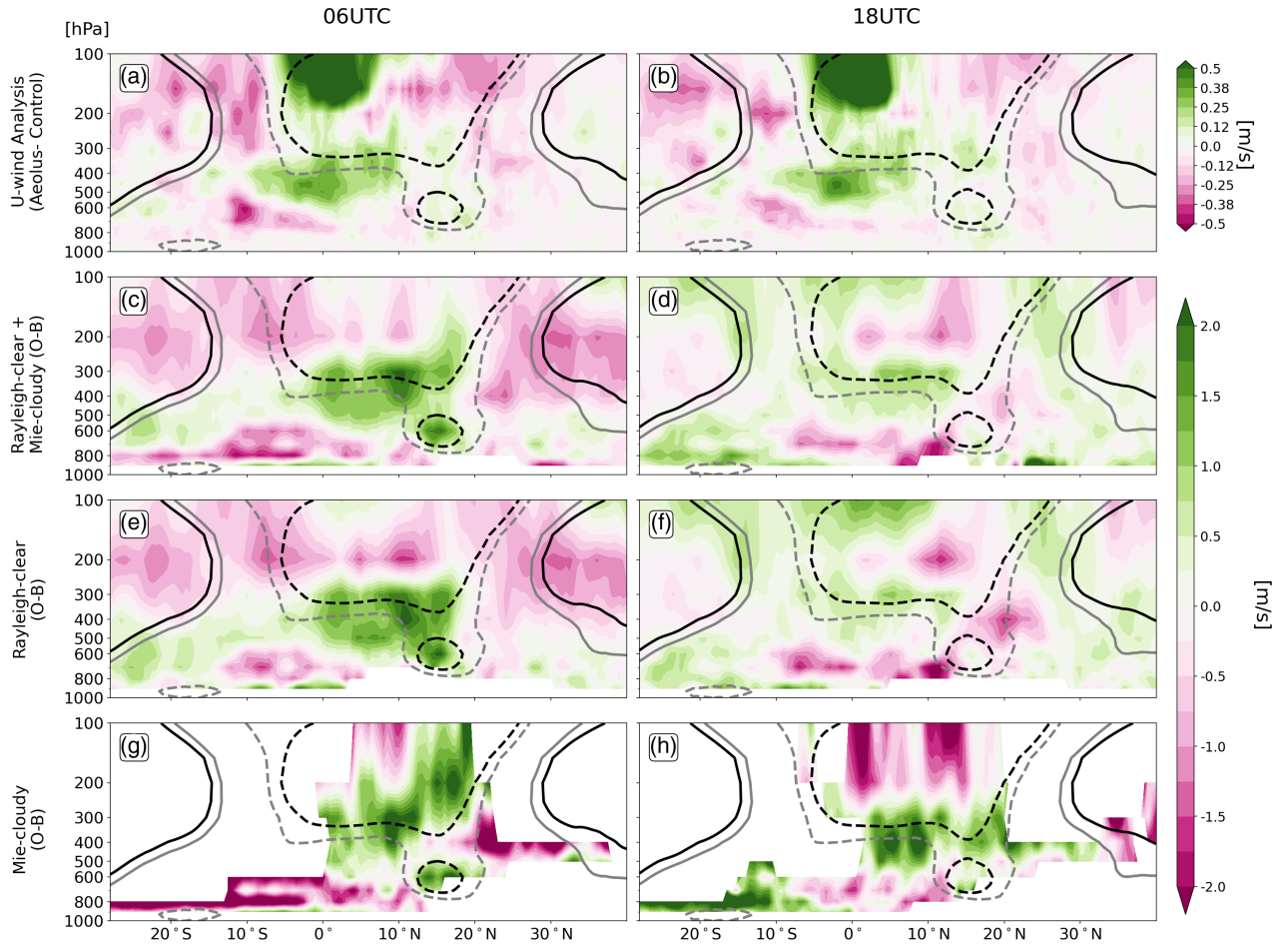

FIGURE 8 As Figure 7 but for the DWD2020 OSE. [Colour figure can be viewed at wileyonlinelibrary.com]

dominated by the Rayleigh-clear signal (Figure 7e,f), particularly in the upper levels. The results suggest an orbital- and vertical-dependent bias that is rather homogeneous with latitude, except maybe near the TEJ where both orbits show the same O−B sign. The Mie-cloudy signal (Figure 7g,h), in contrast, is more consistent between ascending and descending tracks in the convectively active region, while the BB and SAL regions have opposite signs, which is also evident in the combined fields (Figure 7c,d). The reason for this diurnal difference over the aerosol-loaded region is not fully understood and could be related to diurnal wind effects or instrumental factors associated with the presence of aerosols. It is worth noting that, in the area of the TEJ, all channels and orbits show the same sign of departure, which, combined with the assumed low background error (Figure 3h), leaves a strong imprint on the analysis. For the AEJ-North—and particularly its southern flank—the situation is considerably more complicated, with positive differences in Rayleigh-clear at 0600 UTC and Mie-cloudy at 1800 UTC but negative differences in Rayleigh-clear at 1800 UTC and mixed signals in Mie-cloudy at 0600 UTC.

For comparison, Figure 8 shows the same analysis but for the DWD2020 OSE. In stark contrast to ECMWF2020 (Figure 7), the mean analysis differences for morning and evening are almost identical (Figure 8a,b) and thus also agree closely with Figure 4g. Somewhat surprisingly, however, the O−B statistics for Rayleigh-clear and Mie-cloudy combined (Figure 8c,d) show a rather low agreement with the analysis differences. This is particularly true in the upper troposphere and lower stratosphere. The most striking example is the southern part of the TEJ region, where analysis differences are strongly positive, a signal not matched in O−B statistics, particularly not at 0600 UTC. The exact reasons for this discrepancy are not fully understood, but could be related to the background-error covariance in this region, which spreads the observational information in space or through a nonlinear dynamical response in the forecast model. Irrespective of this, the combined O−B data reveal marked diurnal differences that structurally resemble those seen for ECMWF (Figure 7c,d), suggesting that the reason lies in the observations rather than the modelling systems. As for ECMWF, the combined HLOS signals are dominated

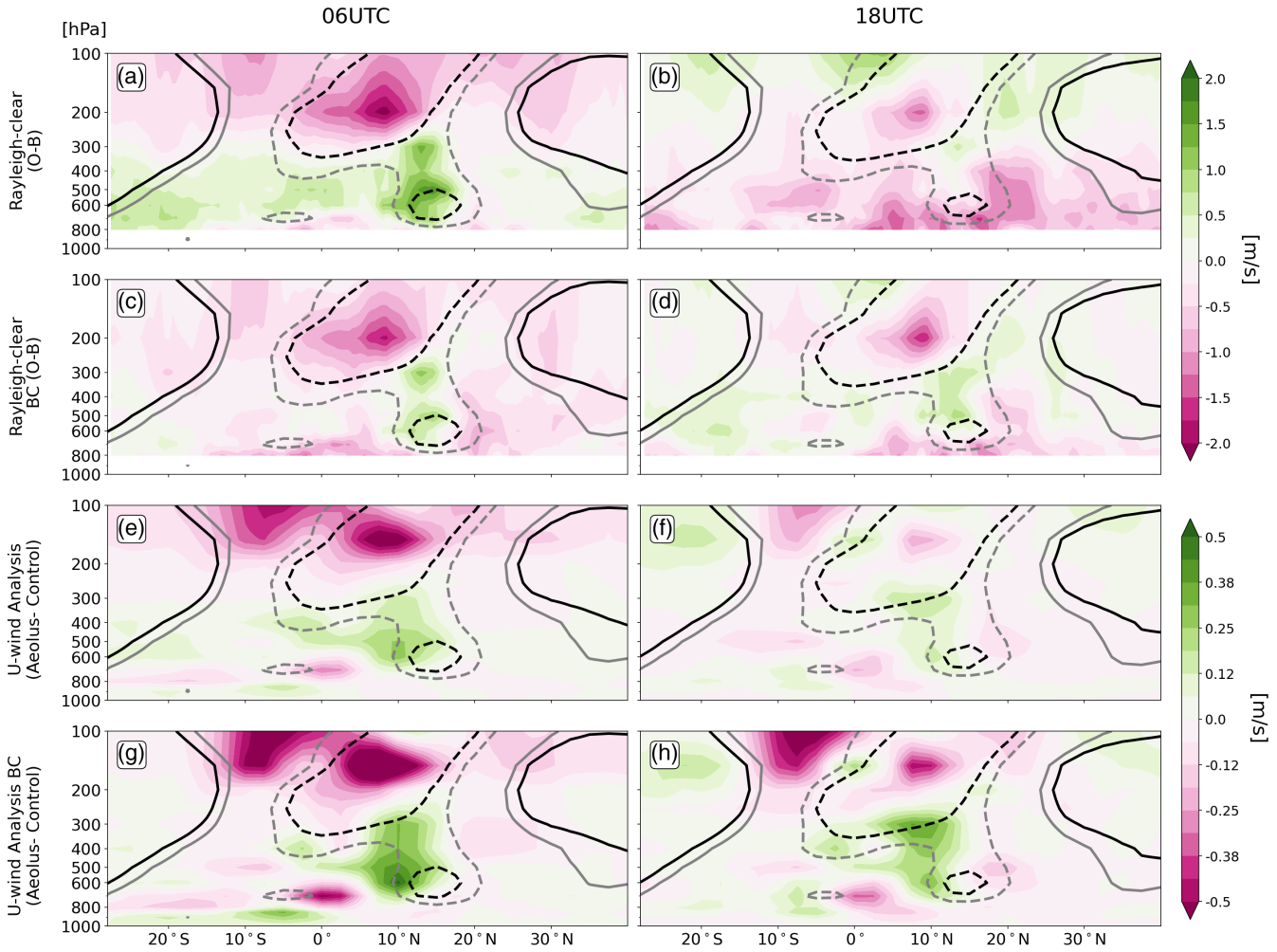

FIGURE 9 Latitude–height cross-sections showing July–September mean HLOS first guess-departures for Rayleigh-clear from the ECMWF2019 OSE with bias-correction (BC, top row) and without BC (second row) at 0600 UTC (left column) and at 1800 UTC (right column). These are analogous to 6e,f for the ECMWF2020 OSE. Corresponding differences between the analysis fields of the zonal wind component *Aeolus* minus Control are shown in the bottom two rows. These are analogous to Figure 6a,b for the ECMWF2020 OSE. All fields are averaged between 30°W and 30°E. The grey and black contours correspond to zonal wind fields of 6 and 9 $m \cdot s^{-1}$, respectively, from the analysis with *Aeolus*. Solid lines indicate westerlies, dashed ones easterlies. HLOS winds from the descending track are multiplied by −1 to correspond with the sign convention of the model coordinate system. [Colour figure can be viewed at wileyonlinelibrary.com]

by the Rayleigh-clear contribution (Figure 8e,f), but for DWD the dominance is even clearer. Ascending and descending tracks are somewhat more consistent than for ECMWF, likely due to the vertical-dependent bias correction used in the DWD2020 OSE. The Mie-cloudy O−B statistics (Figure 8g,h) structurally resemble those in the ECMWF2020 OSE, further supporting the conclusion that the O−B structures found in Figures 6 and 7 are largely independent of the modelling framework used.

Next we will explore to what extent a simple bias correction can cure some of the issues found in the ECMWF system for July–September (JAS) 2020 (see discussion of Figure 7). It was found that the atmospheric temperature is a good predictor for the Rayleigh-clear bias. Therefore, a temperature-dependent bias correction was tested in the ECMWF2019BC OSE (see Table 1). Figure 9 shows the O−B statistics for the Rayleigh-clear channel for the descending and ascending tracks without (ECMWF2019, Figure 9a,b) and with (ECMWF2019BC, Figure 9c,d) bias correction. These figures are analogous to Figure 7e,f, indicating differences between the two years. Particularly for 0600 UTC, the O−B structures are very similar, showing consistency despite the degradation of the instrument, while at 1800 UTC positive differences are evident in the region of the southern STJ and to the south of the northern STJ in 2020, which are much weaker in 2019.

Comparing O−B statistics with and without bias correction (top versus second row in Figure 9) reveals an overall positive effect, reducing the magnitude of the differences almost everywhere. Some regions, mostly in the

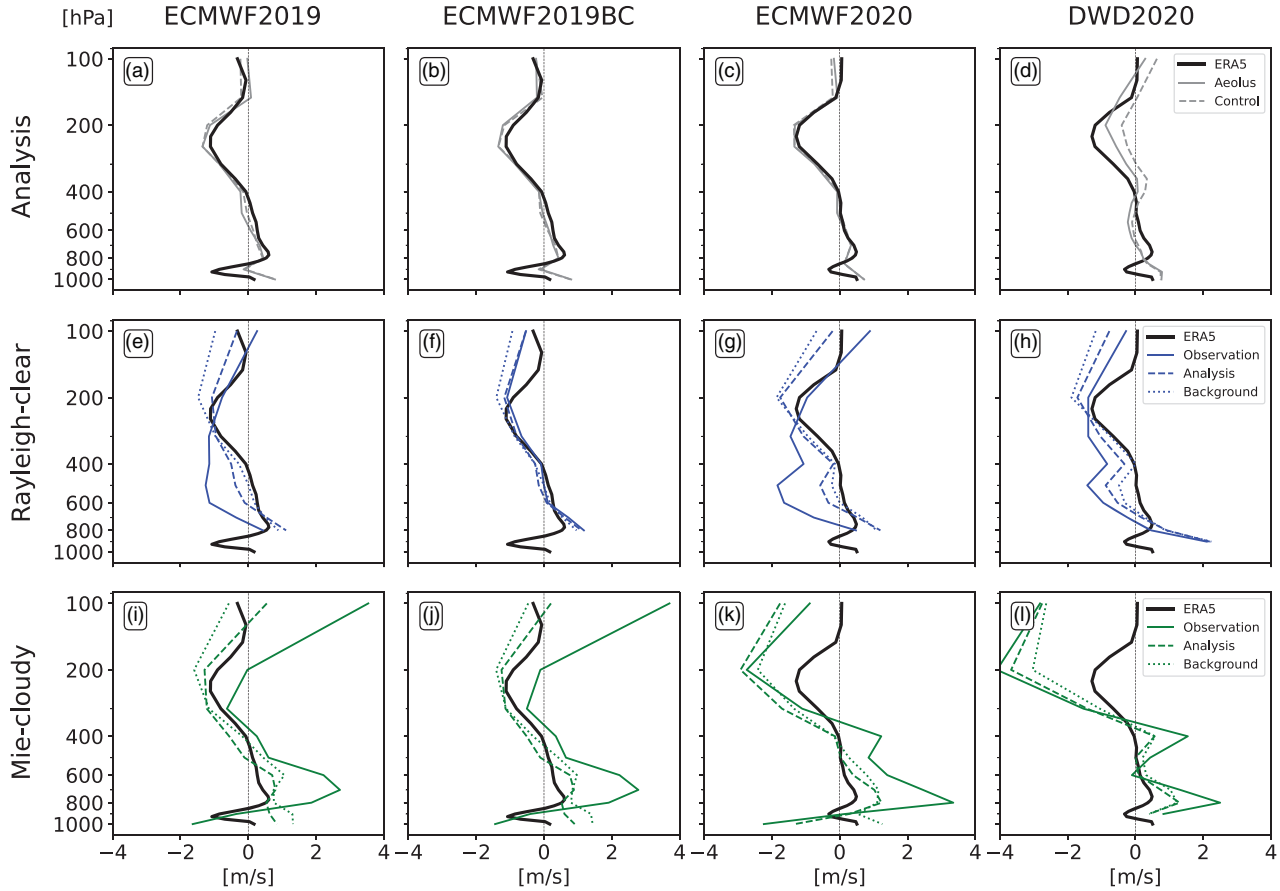

FIGURE 10 Vertical profiles of diurnal differences 1800 UTC minus 0600 UTC of HLOS winds for the four OSEs (Table 1; see column labels) averaged over West Africa (30°W–30°E, 10°S–20°N) during July–September. (a–d) Analysis fields, (e–h) *Aeolus* Rayleigh-clear, and (i–l) Mie-cloudy observations with their analysis and background equivalents. Corresponding fields from the ERA5 reanalysis are plotted in all panels for reference.

lower levels, even change sign, leading to a better agreement between the two tracks. The weaker TEJ signal at 1800 UTC increases somewhat to match that at 0600 UTC better. The temperature-dependent bias correction in the ECMWF2019BC OSE leads to diurnal differences of a similar magnitude to those with the vertical-dependent bias correction applied in the DWD2020 OSE (compare Figure 9c,d with Figure 8e,f).

Figure 9e–h shows the corresponding analysis differences with and without bias correction, in analogy to Figure 7a,b, for JAS 2020. First, comparing the two years with each other, we can see that the analysis impact is generally larger in 2019 than in 2020, particularly at 0600 UTC. This is consistent with the assumed lower observational errors (shading in Figure 3a,b,d,e) and the higher number of counts in 2019 (grey and black lines in the same panels). Comparing O−B statistics (Figure 9a,b) with corresponding analysis differences (Figure 9e,f), first both without bias correction, again shows some structural agreement, but much lower amplitudes in the latter, broadly consistent with the results for 2020 (see Figure 7). Applying the bias correction (Figure 9g,h) clearly amplifies the impact of the *Aeolus* observations on the analysis for both tracks and particularly in and to the south of the TEJ and AEJ-North. This results in a much better agreement of the *Aeolus* effect between ascending and descending orbits, underlying the overall success of the bias correction.

Finally, in order to investigate diurnal patterns further in the different datasets analyzed up to this point, we compare vertical profiles of the mean difference between 1800 UTC and 0600 UTC averaged horizontally over West Africa (10°S–20°N, 30°E–30°W) between the four OSEs (Table 1) and with ERA reanalysis data as a reference (Figure 10). The chosen region is restricted to the low-latitude mean easterly wind features TEJ, AEJ-North, and AEJ-South and excludes the two STJs, but does include the low-level southwesterly monsoon flow (see Figure 2e, for example). Nevertheless, since several wind features are averaged in this region, the diurnal patterns found may be the result of a mixture of different meteorological phenomena. The first row of Figure 10 compares ERA5 reanalysis and OSE analysis fields with and without *Aeolus* data, all projected on the *Aeolus* HLOS. The most prominent feature in ERA5, with an amplitude of more

than 1 m·s^{-1}, occurs at 200 hPa, indicating the strengthening of upper-level easterlies at 1800 UTC, as also observed over northern India in the evening (Krishnamurti and Kishtawal, 2000; Mohan and Rao, 2016), which is related to the diurnal response of convective outflows to surface heating.

Between 800 and 700 hPa, an opposite but much weaker diurnal pattern is apparent, which likely reflects the decrease in wind speed in the AEJ-North (and possibly to a lesser extent AEJ-South) during the afternoon, when the planetary boundary layer grows into the lower parts of the jet and slows it down through turbulent mixing (Agustí-Panareda *et al.,* 2010). Finally, the low-amplitude negative signal around 900 hPa likely reflects the increase of monsoonal westerlies in the course of the night, peaking shortly before sunrise at 0600 UTC (Parker *et al.,* 2005a,b; Kalapureddy *et al.,* 2010; Kalthoff *et al.,* 2018). The diurnal pattern at 1000 hPa should be regarded with some caution, as it will be underground for larger parts of the averaging domain.

In general, the ECMWF analysis fields with (grey solid lines in Figure 10a–c) and without (red solid lines in Figure 10a–c) *Aeolus* data reproduce the ERA5 pattern, except for the ECMWF2020 OSE in the lower troposphere (Figure 10c), where the reanalysis and analysis show some discrepancy. The effect of *Aeolus* on the representation of the diurnal cycle in the analysis fields, however, is at best marginal. For the DWD2020 OSE (Figure 10d), differences between the control analysis and ERA5 are substantially larger, with the former showing a less pronounced diurnal cycle throughout the troposphere. Assimilating *Aeolus* data has a relatively large influence and leads to a better agreement with ERA5, particularly in the TEJ region. This improvement is much more evident from Figure 10 than from the vertical profiles shown in Figure 8a,b.

The second row of Figure 10 compares Rayleigh-clear HLOS observations with their background and analysis counterparts in HLOS space. The diurnal patterns in the background fields in all OSEs (Figure 9e–h, dashed line) are similar to the ERA5 reanalysis below 200 hPa, while above they display stronger easterly winds at 1800 UTC compared with 0600 UTC, suggesting that the Rayleigh-clear HLOS space may be representative of the regional diurnal cycle in the midtroposphere. This is particularly true for the 2019 OSEs, while some inconsistencies around 600 hPa are apparent for the 2020 OSEs. However, the corresponding HLOS observations without temperature-bias correction (blue solid lines in Figure 10e,g,h) do not follow the same diurnal cycle, with a generally stronger easterly component in the midtroposphere at 1800 UTC compared with 0600 UTC, reversing the sign of the expected diurnal cycle of the AEJ-North while still having a realistic representation of the diurnal cycle of the TEJ. The analyses in HLOS space (blue dashed lines) are therefore shifted from the background equivalent towards the HLOS Rayleigh-clear data. When applying the temperature-bias correction as seen in the ECMWF2019BC OSE (Figure 10f), the Rayleigh-clear observation follows an almost identical diurnal cycle to the ERA5 reanalysis and background equivalent, especially below 200 hPa. Correcting for the temperature bias thus has a positive effect on the Rayleigh-clear winds and makes them more realistic in the midtroposphere below 200 hPa.

Finally the bottom row of Figure 10 shows a corresponding analysis for the Mie-cloudy channel. The background HLOS model equivalents in all OSEs (Figure 10i–l, dotted lines) do not follow the ERA5 reanalysis closely, with a more pronounced diurnal cycle near the AEJ-North as well as a stronger TEJ diurnal cycle in 2020 compared with 2019. The magnitude of this discrepancy is generally larger than for Rayleigh-clear data (Figure 10e–g) and related to the fact that the two channels do not measure the same wind properties with the same sampling density as discussed in the context of Figure 3. The diurnal cycle of Mie-cloudy HLOS winds (red dotted lines) in the midtroposphere is opposite to that for the Rayleigh-clear HLOS winds. At upper levels, Mie-cloudy HLOS winds show large positive diurnal differences in 2019 and large positive ones in 2020, with little agreement with the Rayleigh-clear data. As expected, the bias correction applied in ECMWF2019BC has hardly any effect on the Mie-cloudy HLOS winds. The analysis counterparts (red dashed lines) are generally not driven in the direction of the Mie-cloudy observations—sometimes even in the opposite direction—indicating the dominant effect of the Rayleigh-clear data, also found in the analysis of Figure 7. Despite the model differences between ECMWF and DWD, Rayleigh-clear (Figure 9g,h) and Mie-cloudy (Figure 9k,l) behave similarly, as do their model and analysis equivalents.

Exploring background departures of the *Aeolus* HLOS in the DWD and ECMWF assimilation systems enabled us to assess the orbital and channel contribution to the influence on analysis between ascending and descending orbits. We showed the existence of a height- and orbit-dependent bias in the Rayleigh-clear channel that has the effect of accelerating and slowing down the AEJ-North and TEJ diurnally. This bias is a likely explanation for the earlier statement in Section 3.2.1 that the Rayleigh-clear measurements pull the DWD2020 and ECWF2020 analyses apart. This is observed outside the ITCZ region in particular, where the Rayleigh-clear measurements predominate. It should also be noted that even small biases (of the order of 1 m·s^{-1}) can lead to a deterioration of the forecast quality (Horányi *et al.,* 2015). Correcting this bias, using temperature-dependent bias

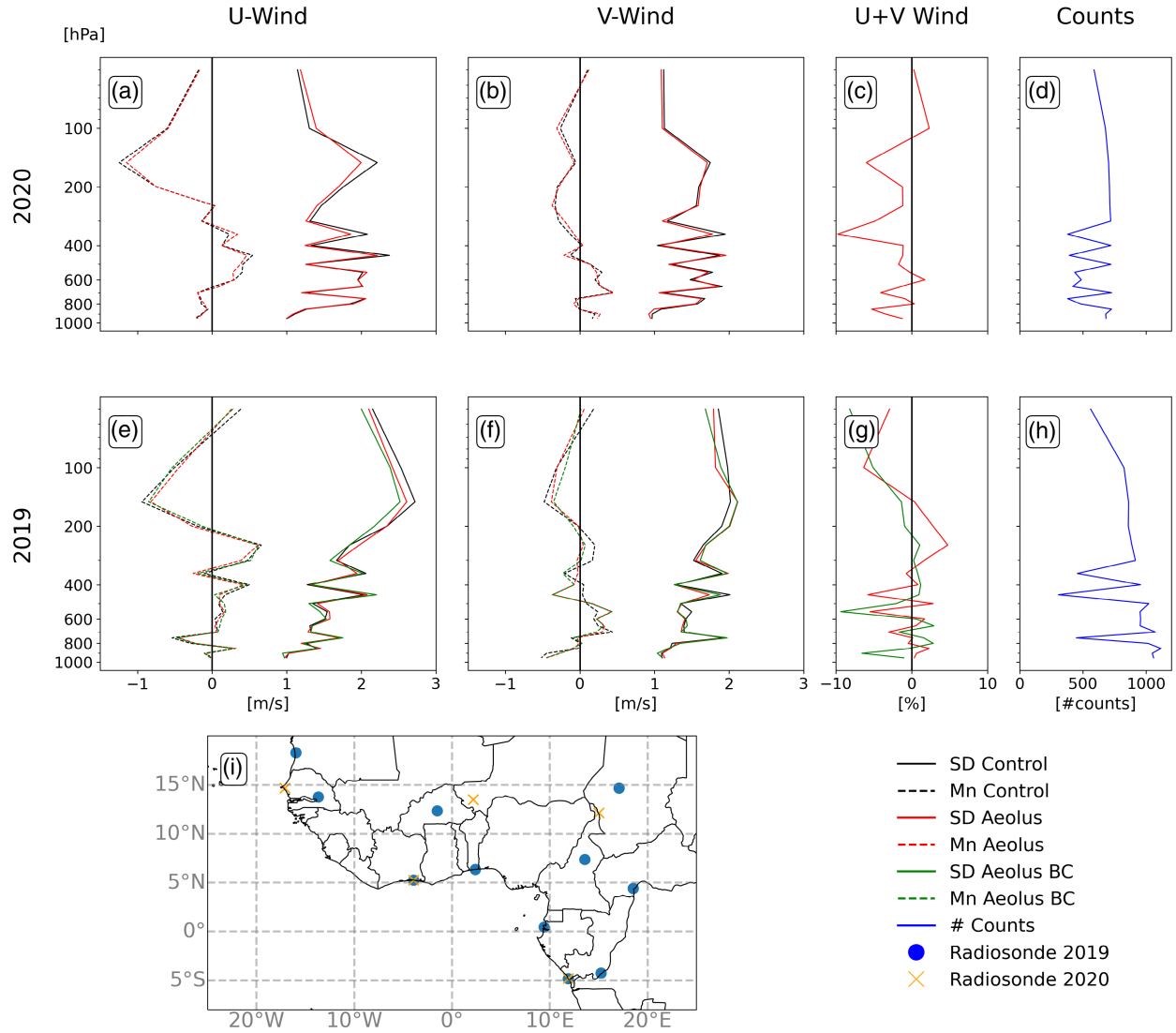

FIGURE 11 Vertical profiles showing July–September mean (Mn) and standard deviation (SD) of radiosonde background departures from *Aeolus* and control experiments of the ECMWF2020 OSE for (a) zonal and (b) meridional winds, (c) relative SD error reduction for the total wind component, and (d) number of reports used to generate the statistics. All fields are averaged over West Africa (20°W–20°E, 10°S–20°N). The second row (e–h) shows corresponding fields for 2019, contrasting the OSEs with and without bias correction (BC). (j) Horizontal map showing the locations of the radiosondes used in 2019 (blue dots) and 2020 (orange crosses). [Colour figure can be viewed at wileyonlinelibrary.com]

corrections, allows for better consistency of Rayleigh-clear winds between ascending and descending orbits. Finally, we showed that the assimilation of *Aeolus* brings the DWD analysis closer to both the ECMWF2020 analysis and the ERA5 reanalysis.

3.3 | Influence on forecast fields

3.3.1 | Background verification against radiosondes

As a first step to understand the impact of *Aeolus* data on forecast fields, this subsection evaluates the background fields from the three ECMWF OSEs with actively assimilated radiosonde measurements using O−B statistics (Figure 11). Corresponding DWD statistics are not shown here, as not enough radiosonde data were assimilated in the OSE to obtain meaningful statistics. In total, 11 and 5 radiosonde stations in tropical Africa were used during July–September 2019 and 2020, respectively (Figure 11i), with only two common stations (Accra in Ghana and Cabinda in Angola). Figure 11d,h shows the number of reports assimilated in the different OSEs, which varies broadly between 500 and 1000 per level, with generally more data in 2019 (~850) than in 2020 (~600). The number of reports is more variable within the lower troposphere.

Figure 11a–c shows the mean O−B difference as well as the standard deviation from the ECMWF2020 OSE for absolute errors in zonal and meridional wind as well as the relative improvement for the total wind speed. The ECMWF first guess has a negative zonal wind bias in the upper troposphere peaking just above 200 hPa at about $-1\,\mathrm{m\cdot s^{-1}}$ (Figure 11a), which indicates a too weak TEJ, as we have shown previously. *Aeolus* reduces this bias to a small extent, in agreement with the analysis impact seen in Figure 4e. There is also a smaller positive bias at midlevels, mostly above 700 hPa, which is barely improved when assimilating *Aeolus* data. The error standard deviation (solid lines in Figure 11a) oscillates around $1.5\,\mathrm{m\cdot s^{-1}}$. Assimilating *Aeolus* wind fields leads to some moderate reductions at upper levels. For meridional wind (Figure 11b), the bias is small throughout the profile and changes little when *Aeolus* is assimilated. The random error has a similar magnitude to that for zonal wind and shows little sensitivity to the (mostly zonal) *Aeolus* measurements. Despite this, the assimilation of *Aeolus* leads to a mass-weighted vertical average random error reduction for the total wind component of 1.95%, which is vertically consistent (Figure 11c).

Figure 11e–g shows the corresponding analysis for 2019 including both OSEs with and without bias correction. The overall patterns agree reasonably well with 2020, despite the large differences in radiosonde data coverage. The most interesting aspect is the effect of the bias correction in ECMWF2019BC. Overall improvements from that are moderate, but some positive effects on the random error in zonal wind and the mean error in meridional wind at upper levels are evident. The vertically averaged relative improvement shown in Figure 11g is overall smaller than in 2020, only 0.45% in the ECMWF2019 OSE and 1.45% in ECMWF2019BC, demonstrating the additional benefit of correcting the Rayleigh-clear wind temperature-dependent bias. This is due in particular to a reduction of the background deterioration with *Aeolus* of around 200 hPa evident in ECMWF2019. Overall, a similar magnitude in the reduction of the background error, peaking in the upper troposphere, was observed in the DACCIWA radiosonde campaign in West Africa in June/July 2016 (van der Linden *et al.*, 2020), suggesting that the assimilation of *Aeolus* has an effect comparable to high-resolution radiosonde coverage over this region in the ECMWF model.

3.3.2 | 1–4 day forecast verification against ERA5 reanalysis

Finally, we will look at the improvements in longer-term forecasts verified with ERA5 over the entire tropical Africa domain. Figures 12 and 13 show the relative reduction of the root-mean-square error (RMSE) of the four OSEs (Table 1) as latitude–height cross-sections for forecast times of 1–4 days and as single levels at 200 and 700 hPa at +48 h forecast time, respectively. As before, isotachs at $6\,\mathrm{m\cdot s^{-1}}$ (grey) and $9\,\mathrm{m\cdot s^{-1}}$ (black) are included to identify the main jet features. In addition, Table 3 provides an overview of the relative improvement of the zonal wind RMSE at 200 and 700 hPa for the whole tropical Africa domain and specifically for the AEJ-North and TEJ regions.

For all OSEs, we see a predominantly positive influence of *Aeolus* data for all forecast lead times. The reduction in RMSE is generally larger for forecast lead times greater than 24 h. In the 2019 ECMWF and DWD2020 OSEs (Figure 12a,b,d), the largest decrease in RMSE at +24 h is found in the lower stratosphere, before vanishing gradually at higher lead times, while in the ECMWF2020 OSE (Figure 12c) the initial errors are more spurious and seem to be preserved at longer lead times. One reason could be the generally poorer quality of the *Aeolus* Rayleigh-clear measurements (Figure 3b) in 2020, compared with 2019, caused by the aforementioned decreasing atmospheric path signal. In the ECMWF2019 OSEs with and without bias correction (Figure 12a,b, Figure 13e,f), the errors at +24 h are found in the Southern Hemisphere at ∼ 700 hPa between 20°S and 0°, which coincides with a change in wind direction between the monsoon layer and the midlevel easterlies. With a bin size of 1 km at this height, *Aeolus* data cannot resolve large vertical gradients and thus may misrepresent the local dynamics. This region also corresponds to a strong increase in the analysis 700 hPa zonal wind of $\sim 0.5\,\mathrm{m\cdot s^{-1}}$ when *Aeolus* is assimilated (Figure 5a,e at 0°). Nevertheless, this large RMSE is, surprisingly, not apparent at 700 hPa in ECMWF2020 and DWD2020 OSE (Figure 13g,h).

Other errors over the SAL region at 20°N are also visible in all OSEs at +24 h, in particular over the lower northern part of the AEJ-North around 800 hPa in the ECMWF OSEs (Figure 12 a,b,c) and the whole northern AEJ-North region in the DWD2020 OSEs (Figure 12d). This includes the Intertropical Discontinuity (ITD), which is a confluence zone between the northeasterly dry and hot Harmattan winds and the southwesterly moist and cool monsoon flow. This pronounced meridional wind feature is challenging to resolve with an *Aeolus* Rayleigh-clear integration length of 87 km.

Furthermore, the AEJ-North is embedded in a dust-loaded region (Figure 1d), which is subject to larger Mie-cloudy (Figure 3d) and Rayleigh-clear assigned observation errors (Figure 3a) due to reduced signal-to-noise ratio. These errors could also be insufficient to compensate fully for the large model errors related to the stochasticity

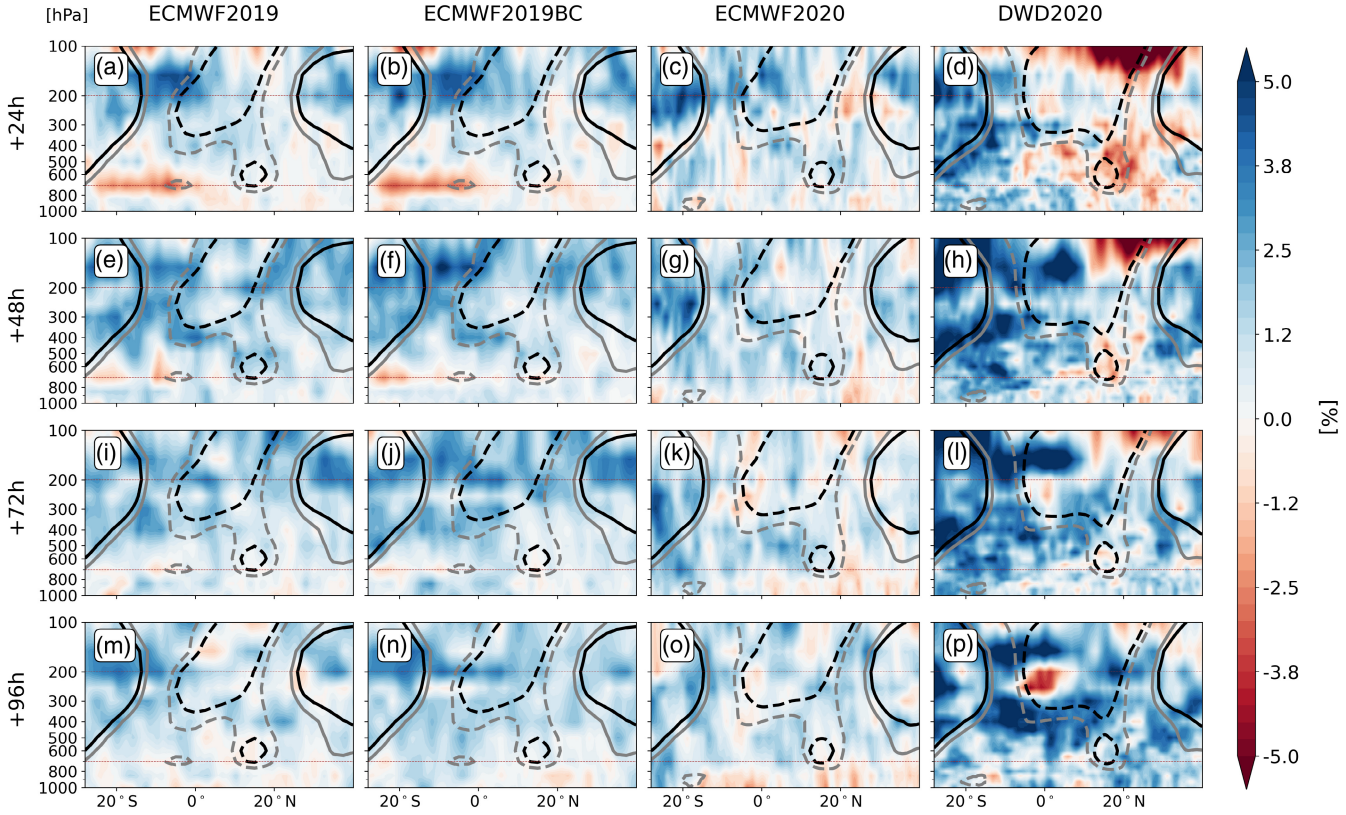

FIGURE 12 Latitude–height cross-sections showing the relative reduction of the RMSE of zonal wind (i.e., (RMSE(CONTROL)−RMSE(AEOLUS))/RMSE(CONTROL)×100) for the four OSEs (Table 1) for +24–96 h lead-time forecasts against ERA5 reanalysis. Cold (warm) colours indicate improvement (degradation) when *Aeolus* is assimilated. All fields are averaged between 30°W and 30°E during July–September. The grey and black contours correspond to zonal wind fields of 6 and 9 $m \cdot s^{-1}$, respectively, from the analysis with *Aeolus*. Solid lines indicate westerlies, dashed ones easterlies. The brown lines mark the 200- and 700-hPa levels. [Colour figure can be viewed at wileyonlinelibrary.com]

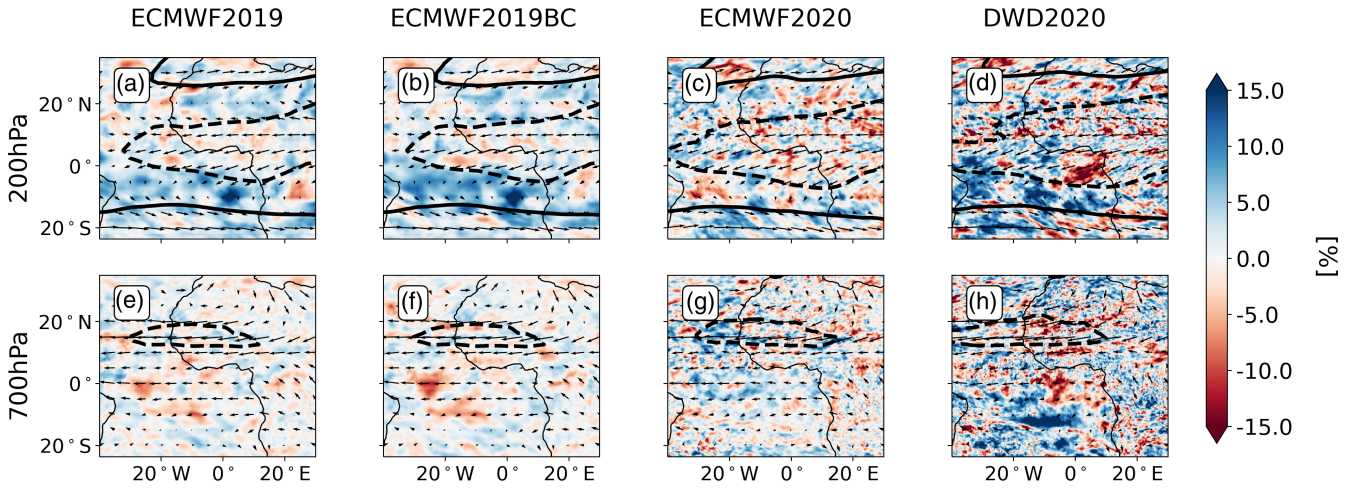

FIGURE 13 Horizontal maps at 200 and 700 hPa showing relative reduction of the RMSE of zonal wind (i.e., (RMSE(CONTROL)−RMSE(AEOLUS))/RMSE(CONTROL)×100) for the four OSEs (Table 1) for +48 h lead-time forecasts against ERA5 reanalysis. Cold (warm) colours indicate improvement (degradation) when *Aeolus* is assimilated. The fields are averaged over July–September. The black contours correspond to zonal wind fields of 9 $m \cdot s^{-1}$, from the analysis with *Aeolus*. Solid lines indicate westerlies, dashed ones easterlies. [Colour figure can be viewed at wileyonlinelibrary.com]

TABLE 3 Overview of the relative reduction of the zonal wind RMSE for the four OSEs (Table 1) in the AEJ-North and TEJ regions for +24–96 h lead-time forecasts verified against ERA5 reanalysis. The fields are averaged within [30°W–30°E; 10°S–20°N] for the TEJ at 200 hPa, [30°W–30°E; 8°N–22°N] for the AEJ-North at 700 hPa, and [30°W–30°E; 30°S–30°N] for comparison at both levels. The values are expressed in percent.

	Lead time	ECMWF2019	ECMWF2019BC	ECMWF2020	DWD2020
	+24 h	+1.98	+2.45	+1.77	+0.74
200 hPa (TEJ)	+48 h	+1.67	+1.89	+1.07	+1.6
[30°W–30°E; 10°S–20°N]	+72 h	+1.77	+2.35	−0.06	+0.89
	+96 h	+1.81	+2.30	−0.10	+0.20
	+24 h	+0.1	+0.01	+0.80	−0.34
700 hPa (AEJ-North)	+48 h	+0.75	+0.24	+1.30	−0.74
[30°W–30°E; 8°N–22°N]	+72 h	+0.37	+0.28	+1.03	−0.78
	+96 h	+0.25	+0.42	+0.22	−0.83
	+24 h	+2.04	+2.39	+1.66	1.51
200 hPa	+48 h	+2.06	+2.42	+1.44	+2.52
[30°W–30°E; 30°S–30°N]	+72 h	+1.97	+2.53	+0.96	+1.34
	+96 h	+1.55	+2.35	+1.09	1.55
	+24 h	−1.4	−1.69	+0.34	−0.06
700 hPa	+48 h	−0.08	−0.44	+0.93	+0.83
[30°W–30°E; 30°S–30°N]	+72 h	+0.09	+0.10	+0.86	1.31
	+96 h	+0.20	+0.52	+0.80	+1.3

of convection and the coupling between atmospheric dynamics and MCSs. However, the general positive influence of *Aeolus* over the AEJ-North region for longer lead times in the ECMWF OSEs (see Table 3) is promising for further studies exploring the impact of *Aeolus* on the propagation of AEWs and related precipitation.

As shown in Table 3, the upper troposphere shows a positive impact for all OSEs with an improvement of more than 2% for most lead times, especially in the southern and northern parts of the TEJ (Figures 12,13), despite being more neutral for the ECMWF2020 OSE. The ECMWF2019BC OSE also shows a systematic improvement in the upper troposphere as well as in the TEJ region, indicating the added value of using a temperature-dependent bias correction for Rayleigh-clear winds. Those regions correspond to cloud-free outer branches of the Hadley cell, while the RMSE is more patchy within the TEJ convective outflow region. The generally better forecast quality in the upper troposphere could possibly be related to the denser sampling together with the smaller measurement uncertainties.

Our findings are consistent with Rennie *et al.* (2021), who have highlighted the benefits of assimilating *Aeolus* wind observations in the Tropics and the Southern Hemisphere, with peak improvements in the tropical upper troposphere. In addition to wind, they also find improvement in other variables such as temperature or humidity. Žagar *et al.* (2021) also reported that the improvement observed in the upper troposphere can be partly attributed to the improvement of the representation of vertically propagating Kelvin waves in layers with a strong zonal wind shear forecast. Lastly, the improvements in the predictions are significant and consistent across the African region, despite the complex meteorology of the WAM and the assumed random errors and biases of the *Aeolus* measurements. Beyond this, it should be noted that the forecast improvement observed in Africa may depend on upstream areas where the influence of *Aeolus* on the analysis is more direct and propagates over time.

4 | CONCLUSIONS

This study addresses the impact of *Aeolus* wind observations on the West African Monsoon (WAM) circulation in the Integrated Forecasting System (IFS) of the European Centre for Medium-Range Weather Forecasts (ECMWF) and the global nonhydrostatic ICOsahedral Model (ICON) of the German Weather Service (DWD). In particular, we investigated the crucial role of *Aeolus* in terms of its ability to complement the sparse conventional observing network and improve the low predictability in this region. The complementary wind observations in clear and cloudy atmospheric conditions are of great importance in a region

with a broad range of cloud features and aerosol types. Accordingly, we assessed and compared the representation of WAM wind subsystems in the analysis and forecast fields of four observing-system experiments (OSEs) across both analysis and forecast fields during the 2019 and 2020 boreal summers. The main conclusions from these investigations are as follows.

1. *Aeolus* Rayleigh-clear and Mie-cloudy channels complement each other well in a complex region like the WAM, which is characterized by many different cloud types and aerosols. Rayleigh-clear samples primarily in cloud-free regions surrounding the Intertropical Convergence Zone (ITCZ) and broken cloud scenes within it, while Mie-cloudy measures in the heart of the convective region across a range of different cloud types such as cumulonimbus, congestus, or altocumulus clouds, as well as aerosols from biomass burning and within the Saharan Air Layer. These different atmospheric components are embedded in the main circulation features of the WAM and allow for a good representation of the midlevel AEJ-North and upper-troposphere TEJ in both channels.
2. The assignment of observation errors for the HLOS wind measurements at ECMWF and DWD is determined using observation minus background (O−B) statistics and Desroziers diagnostics but following different formulations. While ECMWF assumes values based mainly on the L2B processor instrument error combined with representativeness-error estimates, the DWD assigned observation errors are based on a lookup table for different altitude levels. In the ECMWF OSEs, the assigned Rayleigh-clear observation error is largest within the convective active region and can be attributed to a larger signal-to-noise ratio in broken cloud scenes. In the ECMWF2020 OSE, the assigned observation error in the Rayleigh-clear channel is larger compared with 2019 and can be explained by the decreasing atmospheric path signal. For Mie-cloudy, the largest errors are visible in aerosol-dominated regions (BB and SAL) compared with cloudy regions. The overall assigned error for DWD is smaller than for ECMWF, with a general height-dependent error yielding similar values for Mie-cloudy and Rayleigh-clear winds.
3. Throughout the different OSEs, *Aeolus* changes the representation of the main zonal wind features of the WAM. First, a weakening of the southern edge of the AEJ-North is apparent in all ECMWF OSE analyses. This weakening is accompanied by a strengthening of the AEJ-North towards the eastern part of the Sahel in the ECMWF 2019 OSEs. In the DWD OSE, the influence over the AEJ-North is less pronounced. Secondly, the assimilation of *Aeolus* data strengthens the TEJ core by about $0.4\,\mathrm{m\cdot s^{-1}}$ in the ECMWF analyses and, conversely, weakens the southern edge of the TEJ by more than $0.5\,\mathrm{m\cdot s^{-1}}$ in the DWD OSE analysis. This may imply the strengthening/weakening of the updraft in the convective region, leading to more/less divergence in the upper levels, which in turn would affect precipitation in the ECMWF or DWD models, respectively. This will be explored in future studies. Finally, the assimilation of *Aeolus* brings the ECMWF and DWD 2020 analyses closer together, in particular in the upper ITCZ and southern TEJ region, which is dominated by Mie-cloudy measurements and where the systematic differences between DWD and ECMWF zonal winds reach $4\,\mathrm{m\cdot s^{-1}}$. In cloud-free regions, however, the analyses deviate slightly from each other, which may possibly be caused by the additional vertical-dependent bias correction present in the DWD OSE.
4. Background departures were analysed to assess the behaviour of the HLOS observations with respect to the model equivalents and to disentangle the orbital and channel contribution to the observed analysis differences. Primarily, the combined Rayleigh-clear and Mie-cloudy departures show a structure similar to the zonal wind analysis difference. This indicates the presence of a height- and orbit-dependent bias in the Rayleigh-clear channel, which causes the winds to speed up in the morning and slow down in the evening. However, correcting this bias using a temperature-dependent approach shows that the magnitude of this bias is too small to have a significant influence on the analysis and prediction fields. Although this influence is small, the temperature-bias correction provides a better representation of the Rayleigh-clear diurnal winds. Despite the model differences between ECMWF and DWD, both Rayleigh-clear and Mie-cloudy behave similarly with respect to their model equivalents.
5. The ECMWF and DWD zonal wind forecasts verified with ERA5 revealed that *Aeolus* has a positive influence on the WAM zonal winds. The positive impact is most notable in the upper troposphere because of denser observation sampling together with smaller measurement uncertainties. Cloud-free regions exhibit lower RMSE deterioration relative to cloudy regions, owing to the lower signal-to-noise ratio in broken-cloud scenes for Rayleigh-clear winds. Short forecast ranges of +24 h show larger deterioration, possibly due to verification problems in data-sparse regions. Despite the presence of cumulonimbus clouds, the representation of the TEJ is positively impacted by *Aeolus* for most OSEs and lead times. Although the AEJ-North also shows improvement, it is more modest compared with the TEJ and

only apparent in the ECMWF OSEs. This could have implications for the propagation of African Easterly Waves (AEWs) and related Mesoscale Convective Systems (MCSs) in forecasts.

6. The radiosonde verification in the ECMWF OSEs over West Africa showed that the vertically averaged total wind random errors in the 2019 and 2020 OSEs are reduced by 0.45% and 1.95%, respectively, with the effects peaking in the upper troposphere. The reduction of the latter would be comparable to a 1–2 year average reduction in the RMS vector wind error (at 250 and 850 hPa) of the ECMWF +44 h forecast verified against radiosondes in the Tropics (Haiden *et al.,* 2021 their figure 17). The improvement is raised to 1.45% in the 2019 OSE, when a temperature-dependent bias correction in the Rayleigh-clear channel is applied, highlighting the usefulness of the correction.

The influence of *Aeolus* on the forecast quality is positive overall. Through the addition of appropriate bias corrections in the processing chain, *Aeolus* is able to represent the WAM winds in a realistic manner. This is despite the varius remaining complex biases and noise levels in the different channels, which, once corrected, would allow *Aeolus* to reach its full potential. Having investigated the distinct influence of *Aeolus* on key circulation features such as the TEJ and AEJ-North, it remains to be explored how *Aeolus* affects the propagation of AEWs and thus potentially the forecast of tropical cyclones over the downstream Atlantic Ocean (Brammer and Thorncroft, 2015). A positive impact of improving data assimilation in the WAM may also be observed remotely in the midlatitude Euro-Atlantic region (Bielli *et al.,* 2010; Gaetani *et al.,* 2011; Pante and Knippertz, 2019) and the Mediterranean basin (Raicich *et al.,* 2003) through teleconnection effects. There may also be a positive effect on equatorial waves, which are responsible for much of the synoptic and intraseasonal atmospheric variability in the Tropics.

AUTHOR CONTRIBUTIONS

Maurus Borne: conceptualization; data curation; formal analysis; investigation; methodology; software; visualization; writing – original draft. **Peter Knippertz:** conceptualization; methodology; project administration; resources; supervision; writing – original draft. **Martin Weissmann:** conceptualization; methodology; project administration; resources; supervision; writing – original draft. **Anne Martin:** data curation; writing – review and editing. **Michael Rennie:** investigation; software; writing – review and editing. **Alexander Cress:** investigation; software; writing – review and editing.

ACKNOWLEDGEMENTS

This research was carried out within project B6 "New data assimilation approaches to better predict tropical convection" of the Transregional Collaborative Research Centre SFB/ TRR 165 "Waves to Weather", financed by the German Science Foundation (DFG). We acknowledge the European Space Agency (ESA), the European Centre for Medium-Range Weather Forecasts (ECMWF), and the German Weather Service (DWD) for providing the datasets and conducting the observing-system experiments on which this study is based. We also highly appreciate the productive exchanges and mutual support within the Experimental Validation and Assimilation of *Aeolus* observations (EVAA) consortium. Finally, we thank Nedjeljka Žagar and the anonymous reviewers, whose comments helped to improve the quality of the article. Open Access funding enabled and organized by Projekt DEAL.

CONFLICT OF INTEREST STATEMENT

The authors affirm that they have no conflict of interest.

DATA AVAILABILITY STATEMENT

The presented work includes data of the *Aeolus* mission, which is part of the European Space Agency (ESA) Earth Explorer Program, and these data are publicly available at the ESA *Aeolus* Online Dissemination System since May 2020 (https://aeolus-ds.eo.esa.int/oads/access/collection). Some data of the ESA used in this work are not yet publicly released, because they are not fully calibrated/validated. ERA5 data are openly available and can be downloaded from the Copernicus Climate Data Store.

ORCID

Maurus Borne https://orcid.org/0000-0003-4656-5878
Peter Knippertz https://orcid.org/0000-0001-9856-619X
Anne Martin https://orcid.org/0000-0002-8712-5329

REFERENCES

Agustí-Panareda, A., Beljaars, A., Cardinali, C., Genkova, I. and Thorncroft, C. (2010) Impacts of assimilating AMMA soundings on ECMWF analyses and forecasts. *Weather and Forecasting*, 25(4), 1142–1160.

Baker, W.E., Atlas, R., Cardinali, C., Clement, A., Emmitt, G.D., Gentry, B.M., Hardesty, R.M., Källén, E., Kavaya, M.J., Langland, R., Ma, Z., Masutani, M., McCarty, W., Pierce, R.B., Pu, Z., Riishojgaard, L.P., Ryan, J., Tucker, S., Weissmann, M. and Yoe, J.G. (2014) Lidar-measured wind profiles: the missing link in the global observing system. *Bulletin of the American Meteorological Society*, 95(4), 543–564.

Barbosa, P.M., Stroppiana, D., Grégoire, J.M. and Cardoso Pereira, J.M. (1999) An assessment of vegetation fire in Africa (1981–1991): burned areas, burned biomass, and atmospheric emissions. *Global Biogeochemical Cycles*, 13(4), 933–950.

Bayo, O.J. (1985) The separate contributions of line squalls, thunderstorms and the monsoon to the total rainfall in Nigeria. *Journal of Climatology*, 5(5), 543–552.

Becker, T., Bechtold, P. and Sandu, I. (2021) Characteristics of convective precipitation over tropical Africa in storm-resolving global simulations. *Quarterly Journal of the Royal Meteorological Society*, 147(741), 4388–4407.

Benedetti, A., Morcrette, J.J., Boucher, O., Dethof, A., Engelen, R.J., Fisher, M., Flentje, H., Huneeus, N., Jones, L., Kaiser, J.W., Kinne, S., Mangold, A., Razinger, M., Simmons, A.J. and Suttie, M. (2009) Aerosol analysis and forecast in the European Centre for medium-range weather forecasts integrated forecast system: 2 *Data assimilation*. *Journal of Geophysical Research: Atmospheres*, 114(D13). https://doi.org/10.1029/2008JD011235.

Bielli, S., Douville, H. and Pohl, B. (2010) Understanding the west African monsoon variability and its remote effects: an illustration of the grid point nudging methodology. *Climate Dynamics*, 35(1), 159–174.

Bonavita, M., Isaksen, L. and Hólm, E. (2012) On the use of EDA background error variances in the ECMWF 4D-Var. *Quarterly Journal of the Royal Meteorological Society*, 138(667), 1540–1559.

Bouttier, F. and Kelly, G. (2001) Observing-system experiments in the ECMWF 4D-Var data assimilation system. *Quarterly Journal of the Royal Meteorological Society*, 127(574), 1469–1488.

Brammer, A. and Thorncroft, C.D. (2015) Variability and evolution of African easterly wave structures and their relationship with tropical cyclogenesis over the eastern Atlantic. *Monthly Weather Review*, 143(12), 4975–4995.

Burpee, R.W. (1972) The origin and structure of easterly waves in the lower troposphere of North Africa. *Journal of the Atmospheric Sciences*, 29(1), 77–90.

Carter, T.S., Heald, C.L., Cappa, C.D., Kroll, J.H., Campos, T.L., Coe, H., Cotterell, M.I., Davies, N.W., Farmer, D.K., Fox, C., Garofalo, L.A., Hu, L., Langridge, J.M., Levin, E.J.T., Murphy, S.M., Pokhrel, R.P., Shen, Y., Szpek, K., Taylor, J.W. and Wu, H. (2021) Investigating carbonaceous aerosol and its absorption properties from fires in the Western United States (WE-CAN) and southern Africa (ORACLES and CLARIFY). *Journal of Geophysical Research: Atmospheres*, 126(15), e2021JD034984.

Charney, J.G. and Stern, M.E. (1962) On the stability of internal baroclinic jets in a rotating atmosphere. *Journal of Atmospheric Sciences*, 19(2), 159–172.

Cook, K.H. (1999) Generation of the African easterly jet and its role in determining west African precipitation. *Journal of Climate*, 12(5), 1165–1184.

Cress, A. and Wergen, W. (2001) Impact of pro le observations on the German weather Service's NWP system. *Meteorologische Zeitschrift*, 10(2), 91–101.

Dabas, A., Denneulin, M., Flamant, P., Loth, C., Garnier, A. and Dolfi-Bouteyre, A. (2008) Correcting winds measured with a Rayleigh Doppler lidar from pressure and temperature effects. *Tellus A*, 60(2), 206–215.

Desroziers, G., Berre, L., Chapnik, B. and Poli, P. (2005) Diagnosis of observation, background and analysis-error statistics in observation space. *Quarterly Journal of the Royal Meteorological Society*, 131(613), 3385–3396.

Dunion, J.P. and Marron, C.S. (2008) A reexamination of the Jordan mean tropical sounding based on awareness of the Saharan air layer: results from 2002. *Journal of Climate*, 21(20), 5242–5253.

Fink, A., Vincent, D. and Ermert, V. (2006) Rainfall types in the west African Sudanian zone during the summer monsoon 2002. *Monthly Weather Review*, 134(8), 2143–2164.

Fink, A.H., Agustí-Panareda, A., Parker, D.J., Lafore, J.P., Ngamini, J.B., Afiesimama, E., Beljaars, A., Bock, O., Christoph, M., Didé, F., Faccani, C., Fourrié, N., Karbou, F., Polcher, J., Mumba, Z., Nuret, M., Pohle, S., Rabier, F., Tompkins, A.M. and Wilson, G. (2011) Operational meteorology in West Africa: observational networks, weather analysis and forecasting. *Atmospheric Science Letters*, 12(1), 135–141.

Gaetani, M., Pohl, B., Douville, H. and Fontaine, B. (2011) West African monsoon influence on the summer euro-Atlantic circulation. *Geophysical Research Letters*, 38(9). https://doi.org/10.1029/2011GL047150.

Haiden, T., Janousek, M., Vitart, F., Ben-Bouallegue, Z., Ferranti, L., Prates, C., et al. (2021) *Evaluation of ECMWF Forecasts, Including the 2020 Upgrade*, Vol. 880. Reading, UK: ECMWF.

Harnisch, F., Weissmann, M., Cardinali, C. and Wirth, M. (2011) Experimental assimilation of DIAL water vapour observations in the ECMWF global model. *Quarterly Journal of the Royal Meteorological Society*, 137(659), 1532–1546.

Haslett, S.L., Taylor, J.W., Evans, M., Morris, E., Vogel, B., Dajuma, A., Brito, J., Batenburg, A.M., Borrmann, S., Schneider, J., Schulz, C., Denjean, C., Bourrianne, T., Knippertz, P., Dupuy, R., Schwarzenböck, A., Sauer, D., Flamant, C., Dorsey, J., Crawford, I. and Coe, H. (2019) Remote biomass burning dominates southern west African air pollution during the monsoon. *Atmospheric Chemistry and Physics*, 19(24), 15217–15234.

Hersbach, H., Bell, B., Berrisford, P., Hirahara, S., Horányi, A., Muñoz-Sabater, J., Nicolas, J., Peubey, C., Radu, R., Schepers, D., Simmons, A., Soci, C., Abdalla, S., Abellan, X., Balsamo, G., Bechtold, P., Biavati, G., Bidlot, J., Bonavita, M., Chiara, G., Dahlgren, P., Dee, D., Diamantakis, M., Dragani, R., Flemming, J., Forbes, R., Fuentes, M., Geer, A., Haimberger, L., Healy, S., Hogan, R.J., Hólm, E., Janisková, M., Keeley, S., Laloyaux, P., Lopez, P., Lupu, C., Radnoti, G., Rosnay, P., Rozum, I., Vamborg, F., Villaume, S. and Thépaut, J.N. (2020) The ERA5 global reanalysis. *Quarterly Journal of the Royal Meteorological Society*, 146(730), 1999–2049.

Hollingsworth, A., Shaw, D., Lönnberg, P., Illari, L., Arpe, K. and Simmons, A. (1986) Monitoring of observation and analysis quality by a data assimilation system. *Monthly Weather Review*, 114(5), 861–879.

Horányi, A., Cardinali, C., Rennie, M. and Isaksen, L. (2015) The assimilation of horizontal line-of-sight wind information into the ECMWF data assimilation and forecasting system. Part II: the impact of degraded wind observations. *Quarterly Journal of the Royal Meteorological Society*, 141(689), 1233–1243.

Hunt, B.R., Kostelich, E.J. and Szunyogh, I. (2007) Efficient data assimilation for spatiotemporal chaos: a local ensemble transform Kalman filter. *Physica D: Nonlinear Phenomena*, 230(1-2), 112–126.

Janiga, M.A. and Thorncroft, C.D. (2016) The influence of African easterly waves on convection over tropical Africa and the East Atlantic. *Monthly Weather Review*, 144(1), 171–192.

Johnson, R.H., Rickenbach, T.M., Rutledge, S.A., Ciesielski, P.E. and Schubert, W.H. (1999) Trimodal characteristics of tropical convection. *Journal of Climate*, 12(8), 2397–2418.

Kalapureddy, M., Lothon, M., Campistron, B., Lohou, F. and Saı¨d, F. (2010) Wind profiler analysis of the African easterly jet in relation with the boundary layer and the Saharan heat-low.

Quarterly Journal of the Royal Meteorological Society, 136(S1), 77–91.

Kalthoff, N., Lohou, F., Brooks, B., Jegede, G., Adler, B., Babić, K., Dione, C., Ajao, A., Amekudzi, L.K., Aryee, J.N.A., Ayoola, M., Bessardon, G., Danuor, S.K., Handwerker, J., Kohler, M., Lothon, M., Pedruzo-Bagazgoitia, X., Smith, V., Sunmonu, L., Wieser, A., Fink, A.H. and Knippertz, P. (2018) An overview of the diurnal cycle of the atmospheric boundary layer during the west African monsoon season: results from the 2016 observational campaign. *Atmospheric Chemistry and Physics*, 18(4), 2913–2928.

Kamga, A.F., Fongang, S. and Viltard, A. (2000) Systematic errors of the ECMWF operational model over tropical Africa. *Monthly Weather Review*, 128(6), 1949–1959.

Kelly, G., McNally, T., Thépaut, J. and Szyndel, M. (2004) OSEs of all main data types in the ECMWF operation system. In: *Proceedings of the Third WMO Workshop on the Impact of Various Observing Systems on Numerical Weather Prediction*, pp. 63–94. Reading, UK: ECMWF.

Knippertz, P., Fink, A.H., Deroubaix, A., Morris, E., Tocquer, F., Evans, M.J., Flamant, C., Gaetani, M., Lavaysse, C., Mari, C., Marsham, J.H., Meynadier, R., Affo-Dogo, A., Bahaga, T., Brosse, F., Deetz, K., Guebsi, R., Latifou, I., Maranan, M., Rosenberg, P.D. and Schlueter, A. (2017) A meteorological and chemical overview of the DACCIWA field campaign in West Africa in June–July 2016. *Atmospheric Chemistry and Physics*, 17(17), 10893–10918.

Knippertz, P., Fink, A.H., Schuster, R., Trentmann, J., Schrage, J.M. and Yorke, C. (2011) Ultra-low clouds over the southern west African monsoon region. *Geophysical Research Letters*, 38(21). https://doi.org/10.1029/2011GL049278.

Krisch, I., Lemmerz, C., Lux, O., Marksteiner, U., Masoumzadeh, N., Reitebuch, O., et al. (2020) Data quality of Aeolus wind measurements. *Geophysical Research Abstracts*. https://doi.org/10.5194/egusphere-egu2020-9471.

Krishnamurthy, P., Lewis, K. and Choularton, R. (2014) A methodological framework for rapidly assessing the impacts of climate risk on national-level food security through a vulnerability index. *Global Environmental Change*, 25, 121–132.

Krishnamurti, T. and Kishtawal, C. (2000) A pronounced continental-scale diurnal mode of the Asian summer monsoon. *Monthly Weather Review*, 128(2), 462–473.

Lemburg, A., Bader, J. and Claussen, M. (2019) Sahel rainfall–tropical easterly jet relationship on synoptic to intraseasonal time scales. *Monthly Weather Review*, 147(5), 1733–1752.

Levin, E.J.T., McMeeking, G.R., Carrico, C.M., Mack, L.E., Kreidenweis, S.M., Wold, C.E., Moosmüller, H., Arnott, W.P., Hao, W.M., Collett, J.L., Jr. and Malm, W.C. (2010) Biomass burning smoke aerosol properties measured during fire Laboratory at Missoula Experiments (FLAME). *Journal of Geophysical Research: Atmospheres*, 115(D18). https://doi.org/10.1029/2009JD013601.

Lux, O., Wernham, D., Bravetti, P., McGoldrick, P., Lecrenier, O., Riede, W., D'Ottavi, A., de Sanctis, V., Schillinger, M., Lochard, J., Marshall, J., Lemmerz, C., Weiler, F., Mondin, L., Ciapponi, A., Kanitz, T., Elfving, A., Parrinello, T. and Reitebuch, O. (2020) High-power and frequency-stable ultraviolet laser performance in space for the wind lidar on Aeolus. *Optics Letters*, 45(6), 1443–1446.

Marseille, G. and Stoffelen, A. (2003) Simulation of wind profiles from a space-borne Doppler wind LIDAR. *Quarterly Journal of the Royal Meteorological Society*, 129(594), 3079–3098.

Martin, A., Weissmann, M., Reitebuch, O., Rennie, M., Geiß, A. and Cress, A. (2020) Validation of Aeolus winds using radiosonde observations and NWP model equivalents. *Atmospheric Measurement Techniques Discussions*, 1–24. https://doi.org/10.5194/amt-14-2167-2021

Mathon, V., Laurent, H. and Lebel, T. (2002) Mesoscale convective system rainfall in the Sahel. *Journal of Applied Meteorology*, 41(11), 1081–1092.

Mohan, T. and Rao, T. (2016) Differences in the mean wind and its diurnal variation between wet and dry spells of the monsoon over Southeast India. *Journal of Geophysical Research: Atmospheres*, 121(12), 6993–7006.

Mohr, K.I. and Thorncroft, C.D. (2006) Intense convective systems in West Africa and their relationship to the African easterly jet. *Quarterly Journal of the Royal Meteorological Society*, 132(614), 163–176.

Morcrette, J.J., Boucher, O., Jones, L., Salmond, D., Bechtold, P., Beljaars, A., Benedetti, A., Bonet, A., Kaiser, J.W., Razinger, M., Schulz, M., Serrar, S., Simmons, A.J., Sofiev, M., Suttie, M., Tompkins, A.M. and Untch, A. (2009) Aerosol analysis and forecast in the European Centre for medium-range weather forecasts integrated forecast system: forward modeling. *Journal of Geophysical Research: Atmospheres*, 114(D6). https://doi.org/10.1029/2008JD011235.

Nicholson, S.E. (2009) A revised picture of the structure of the "monsoon" and land ITCZ over West Africa. *Climate Dynamics*, 32(7), 1155–1171.

Nicholson, S.E. and Grist, J.P. (2003) The seasonal evolution of the atmospheric circulation over West Africa and equatorial Africa. *Journal of Climate*, 16(7), 1013–1030.

Pante, G. and Knippertz, P. (2019) Resolving Sahelian thunderstorms improves mid-latitude weather forecasts. *Nature Communications*, 10(1), 1–9.

Parker, D.J., Burton, R.R., Diongue-Niang, A., Ellis, R.J., Felton, M., Taylor, C.M., Thorncroft, C.D., Bessemoulin, P. and Tompkins, A.M. (2005b) The diurnal cycle of the west African monsoon circulation. *Quarterly Journal of the Royal Meteorological Society*, 131(611), 2839–2860.

Parker, D.J., Fink, A., Janicot, S., Ngamini, J.B., Douglas, M., Afiesimama, E., Agusti-Panareda, A., Beljaars, A., Dide, F., Diedhiou, A., Lebel, T., Polcher, J., Redelsperger, J.L., Thorncroft, C. and Wilson, G.A. (2008) The AMMA radiosonde program and its implications for the future of atmospheric monitoring over Africa. *Bulletin of the American Meteorological Society*, 89(7), 1015–1028.

Parker, D.J., Thorncroft, C.D., Burton, R.R. and Diongue-Niang, A. (2005a) Analysis of the African easterly jet, using aircraft observations from the JET2000 experiment. *Quarterly Journal of the Royal Meteorological Society*, 131(608), 1461–1482.

Rabier, F., Järvinen, H., Klinker, E., Mahfouf, J.F. and Simmons, A. (2000) The ECMWF operational implementation of four-dimensional variational assimilation. I: experimental results with simplified physics. *Quarterly Journal of the Royal Meteorological Society*, 126(564), 1143–1170.

Raicich, F., Pinardi, N. and Navarra, A. (2003) Teleconnections between Indian monsoon and Sahel rainfall and the Mediterranean. *International Journal of Climatology: A Journal of the Royal Meteorological Society*, 23(2), 173–186.

Reid, J., Koppmann, R., Eck, T. and Eleuterio, D. (2005) A review of biomass burning emissions part II: intensive physical properties

of biomass burning particles. *Atmospheric Chemistry and Physics*, 5(3), 799–825.

Reitebuch, O. (2012) The spaceborne wind lidar mission ADM-Aeolus. In: *Atmospheric Physics*. Berlin, Heidelberg: Springer, pp. 815–827.

Reitebuch, O., Lemmerz, C., Lux, O., Marksteiner, U., Krisch, I., Masoumzadeh, N., et al. (2020) *Assessment of the Aeolus Performance and Bias Correction-Results from the Aeolus DISC*. DLR. Available at: https://elib.dlr.de/138648/.

Reitebuch, O., Lemmerz, C., Lux, O., Marksteiner, U., Rahm, S., Weiler, F., et al. (2019) Initial assessment of the performance of the first wind lidar in space on Aeolus. In: *EPJ Web of Conferences*, Vol. 237, pp. 1–4. https://doi.org/10.1051/epjconf/202023701010.

Rennie, M., Tan, D., Poli, P., Dabas, A., De Kloe, J., Marseille, G.J. and Stoffelen, A. (2020) Aeolus level-2B algorithm theoretical basis document, ECMWF. *Quarterly Journal of the Royal Meteorological Society* Available at: https://earth.esa.int/eogateway/documents/20142/37627/Aeolus-L2B-Algorithm-ATBD.pdf.

Rennie, M.P., Isaksen, L., Weiler, F., de Kloe, J., Kanitz, T. and Reitebuch, O. (2021) The impact of Aeolus wind retrievals on ECMWF global weather forecasts. *Quarterly Journal of the Royal Meteorological Society*, 147(740), 3555–3586.

Schindler, M., Weissmann, M., Schäfler, A. and Radnoti, G. (2020) The impact of Dropsonde and extra radiosonde observations during NAWDEX in autumn 2016. *Monthly Weather Review*, 148(2), 809–824.

Schlueter, A., Fink, A.H. and Knippertz, P. (2019b) A systematic comparison of tropical waves over northern Africa. Part II: dynamics and thermodynamics. *Journal of Climate*, 32(9), 2605–2625.

Schlueter, A., Fink, A.H., Knippertz, P. and Vogel, P. (2019a) A systematic comparison of tropical waves over northern Africa. Part I: influence on rainfall. *Journal of Climate*, 32(5), 1501–1523.

Schraff, C., Reich, H., Rhodin, A., Schomburg, A., Stephan, K., Periáñez, A. and Potthast, R. (2016) Kilometre-scale ensemble data assimilation for the COSMO model (KENDA). *Quarterly Journal of the Royal Meteorological Society*, 142(696), 1453–1472.

Schrage, J.M. and Fink, A.H. (2012) Nocturnal continental low-level stratus over tropical West Africa: observations and possible mechanisms controlling its onset. *Monthly Weather Review*, 140(6), 1794–1809.

Senior, C.A., Marsham, J.H., Berthou, S., Burgin, L.E., Folwell, S.S., Kendon, E.J., Klein, C.M., Jones, R.G., Mittal, N., Rowell, D.P., Tomassini, L., Vischel, T., Becker, B., Birch, C.E., Crook, J., Dougill, A.J., Finney, D.L., Graham, R.J., Hart, N.C.G., Jack, C.D., Jackson, L.S., James, R., Koelle, B., Misiani, H., Mwalukanga, B., Parker, D.J., Stratton, R.A., Taylor, C.M., Tucker, S.O., Wainwright, C.M., Washington, R. and Willet, M.R. (2021) Convection-permitting regional climate change simulations for understanding future climate and informing decision-making in Africa. *Bulletin of the American Meteorological Society*, 102(6), E1206–E1223.

Stoffelen, A., Marseille, G.J., Bouttier, F., Vasiljevic, D., De Haan, S. and Cardinali, C. (2006) ADM-Aeolus Doppler wind lidar observing system simulation experiment. *Quarterly Journal of the Royal Meteorological Society*, 132(619), 1927–1947.

Stoffelen, A., Pailleux, J., Källén, E., Vaughan, J.M., Isaksen, L., Flamant, P., et al. (2005) The atmospheric dynamics mission for global wind field measurement. *Bulletin of the American Meteorological Society*, 86(1), 73–88.

Thorncroft, C. and Blackburn, M. (1999) Maintenance of the African easterly jet. *Quarterly Journal of the Royal Meteorological Society*, 125(555), 763–786.

Tompkins, A., Cardinali, C., Morcrette, J.J. and Rodwell, M. (2005a) Influence of aerosol climatology on forecasts of the African easterly jet. *Geophysical Research Letters*, 32(10). https://doi.org/10.1029/2004GL022189.

Tompkins, A., Diongue-Niang, A., Parker, D. and Thorncroft, C. (2005b) The African easterly jet in the ECMWF integrated forecast system: 4D-Var analysis. *Quarterly Journal of the Royal Meteorological Society*, 131(611), 2861–2885.

van der Linden, R., Knippertz, P., Fink, A.H., Ingleby, B., Maranan, M. and Benedetti, A. (2020) The influence of DACCIWA radiosonde data on the quality of ECMWF analyses and forecasts over southern West Africa. *Quarterly Journal of the Royal Meteorological Society*, 146(729), 1719–1739.

Vogel, P., Knippertz, P., Fink, A.H., Schlueter, A. and Gneiting, T. (2018) Skill of global raw and postprocessed ensemble predictions of rainfall over northern tropical Africa. *Weather and Forecasting*, 33(2), 369–388.

Vogel, P., Knippertz, P., Gneiting, T., Fink, A.H., Klar, M. and Schlueter, A. (2021) Statistical forecasts for the occurrence of precipitation outperform global models over northern tropical Africa. *Geophysical Research Letters*, 48(3), e2020GL091022.

Walz, E.M., Maranan, M., van der Linden, R., Fink, A.H. and Knippertz, P. (2021) An IMERG-based optimal extended probabilistic climatology (EPC) as a benchmark ensemble forecast for precipitation in the tropics and subtropics. *Weather and Forecasting*, 36(4), 1561–1573.

Weiler, F., Kanitz, T., Wernham, D., Rennie, M., Huber, D., Schillinger, M., et al. (2020) Characterization of dark current signal measurements of the ACCDs used on-board the Aeolus satellite. *Atmospheric Measurement Techniques Discussions*, 1–39. https://doi.org/10.5194/amt-14-5153-2021.

Weiler, F., Rennie, M., Kanitz, T., Isaksen, L., Checa, E., de Kloe, J., Okunde, N. and Reitebuch, O. (2021) Correction of wind bias for the lidar on board Aeolus using telescope temperatures. *Atmospheric Measurement Techniques*, 14(11), 7167–7185.

Weissmann, M., Busen, R., Dörnbrack, A., Rahm, S. and Reitebuch, O. (2005) Targeted observations with an airborne wind LIDAR. *Journal of Atmospheric and Oceanic Technology*, 22(11), 1706–1719.

Weissmann, M. and Cardinali, C. (2007) Impact of airborne Doppler lidar observations on ECMWF forecasts. *Quarterly Journal of the Royal Meteorological Society*, 133(622), 107–116.

Weissmann, M., Harnisch, F., Wu, C.C., Lin, P.H., Ohta, Y., Yamashita, K., Kim, Y.H., Jeon, E.H., Nakazawa, T. and Aberson, S. (2011) The influence of assimilating Dropsonde data on typhoon track and Midlatitude forecasts. *Monthly Weather Review*, 139(3), 908–920.

Weissmann, M., Langland, R.H., Cardinali, C., Pauley, P.M. and Rahm, S. (2012) Influence of airborne Doppler wind lidar profiles near typhoon Sinlaku on ECMWF and NOGAPS forecasts. *Quarterly Journal of the Royal Meteorological Society*, 138(662), 118–130.

Žagar, N. (2004) Assimilation of equatorial waves by line-of-sight wind observations. *Journal of the Atmospheric Sciences*, 61(15), 1877–1893.

Žagar, N., Rennie, M. and Isaksen, L. (2021) Uncertainties in kelvin waves in ECMWF analyses and forecasts: insights from Aeolus observing system experiments. *Geophysical Research Letters*, 48(22), e2021GL094716.

Žagar, N., Stoffelen, A., Marseille, G.J., Accadia, C. and Schlüssel, P. (2008) Impact assessment of simulated Doppler wind LIDARS with a multivariate variational assimilation in the tropics. *Monthly Weather Review*, 136(7), 2443–2460.

Zängl, G., Reinert, D., Rípodas, P. and Baldauf, M. (2015) The ICON (ICOsahedral non-hydrostatic) modelling framework of DWD and MPI-M: description of the non-hydrostatic dynamical core. *Quarterly Journal of the Royal Meteorological Society*, 141(687), 563–579.

Zapotocny, T.H., Menzel, W.P., Nelson, J.P., III and Jung, J.A. (2002) An impact study of five remotely sensed and five in situ data types in the eta data assimilation system. *Weather and Forecasting*, 17(2), 263–285.

Zuidema, P., Redemann, J., Haywood, J., Wood, R., Piketh, S., Hipondoka, M. and Formenti, P. (2016) Smoke and clouds above the Southeast Atlantic: upcoming field campaigns probe absorbing aerosol's impact on climate. *Bulletin of the American Meteorological Society*, 97(7), 1131–1135.

How to cite this article: Borne, M., Knippertz, P., Weissmann, M., Martin, A., Rennie, M. & Cress, A. (2023) Impact of *Aeolus* wind lidar observations on the representation of the West African monsoon circulation in the ECMWF and DWD forecasting systems. *Quarterly Journal of the Royal Meteorological Society*, 149(752), 933–958. Available from: https://doi.org/10.1002/qj.4442